A&A 591, A48 (2016)
DOI: 10.1051/0004-6361/201528045

Astronomy & Astrophysics

Nearby supernova host galaxies from the CALIFA survey

II. Supernova environmental metallicity

L. Galbany[1,2], V. Stanishev[3], A. M. Mourão[3], M. Rodrigues[4,5], H. Flores[5], C. J. Walcher[6], S. F. Sánchez[7], R. García-Benito[8], D. Mast[9], C. Badenes[10], R. M. González Delgado[8], C. Kehrig[8], M. Lyubenova[11], R. A. Marino[12,13], M. Mollá[14], S. Meidt[15], E. Pérez[8], G. van de Ven[15], and J. M. Vílchez[8]

[1] Millennium Institute of Astrophysics, Santiago, Chile
e-mail: lgalbany@das.uchile.cl
[2] Departamento de Astronomía, Universidad de Chile, Casilla 36-D, Santiago, Chile
[3] CENTRA – Centro Multidisciplinar de Astrofísica and Departamento de Física, Instituto Superior Técnico, ULisboa, Av. Rovisco Pais 1, 1049-001 Lisbon, Portugal
[4] European Southern Observatory, Alonso de Cordova 3107 Casilla 19001 – Vitacura – Santiago, Chile
[5] GEPI, Observatoire de Paris, UMR 8111, CNRS, Université Paris Diderot, 5 place Jules Janssen, 92190 Meudon, France
[6] Leibniz-Institut für Astrophysik Potsdam (AIP), An der Sternwarte 16, 14482 Potsdam, Germany
[7] Instituto de Astronomía, Universidad Nacional Autónoma de México, A.P. 70-264, 04510 México, D.F., Mexico
[8] Instituto de Astrofsica de Andalucía (CSIC), Glorieta de la Astronomía s/n, Aptdo. 3004, 18080 Granada, Spain
[9] Instituto de Cosmologia, Relatividade e Astrofísica – ICRA, Centro Brasileiro de Pesquisas Físicas, Rua Dr. Xavier Sigaud 150, CEP, 22290-180 Rio de Janeiro, RJ, Brazil
[10] Department of Physics and Astronomy, University of Pittsburgh, Allen Hall, 3941 O'Hara St, Pittsburgh PA 15260, USA
[11] Kapteyn Astronomical Institute, University of Groningen, PO Box 800, 9700 AV Groningen, The Netherlands
[12] Department of Physics, Institute for Astronomy, ETH Zürich, 8093 Zürich, Switzerland
[13] Departamento de Astrofísica y CC. de la Atmósfera, Facultad de CC. Físicas, Universidad Complutense de Madrid, Avda. Complutense s/n, 28040 Madrid, Spain
[14] Departamento de Investigación Básica, CIEMAT, Avda. Complutense 40, 28040 Madrid, Spain
[15] Max-Planck-Institut für Astronomie / Königstuhl 17, 69117 Heidelberg, Germany

Received 25 December 2015 / Accepted 15 April 2016

ABSTRACT

The metallicity of a supernova progenitor, together with its mass, is one of the main parameters that can rule the progenitor's fate. We present the second study of nearby supernova (SN) host galaxies ($0.005 < z < 0.03$) using integral field spectroscopy (IFS) from the CALIFA survey. We analyze the metallicity of 115 galaxies, which hosted 132 SNe within and 10 SNe outside the field of view (FoV) of the instrument. Another 18 galaxies, which hosted only SNe outside the FoV, were also studied. Using the O3N2 calibrator that was described elsewhere, we found no statistically significant differences between the gas-phase metallicities at the locations of the three main SN types – Ia, Ib/c and II; they all have $12 + \log(\mathrm{O/H}) \simeq 8.50$ within 0.02 dex. The total galaxy metallicities are also very similar, and we argue that the reason is that our sample only consists of SNe discovered in massive galaxies ($\log(M/M_{\odot}) > 10$ dex) by targeted searches. We neither found evidence that the metallicity at the SN location differs from the average metallicity at the galactocentric distance of the SNe. By extending our SN sample with published metallicities at the SN location, we are able to study the metallicity distributions for all SN subtypes split into SN discovered in targeted and untargeted searches. We confirm a bias toward higher host masses and metallicities in the targeted searches. By combining data from targeted and untargeted searches, we found a sequence from higher to lower local metallicity: SN Ia, Ic, and II show the highest metallicity, which is significantly higher than those of SN Ib, IIb, and Ic-BL. Our results support the scenario according to which SN Ib result from binary progenitors. Additionally, at least part of the SN Ic are the result of single massive stars that were stripped of their outer layers by metallicity-driven winds. We studied several proxies of the local metallicity that are frequently used in the literature and found that the total host metallicity allows estimating the metallicity at the SN location with an accuracy better than 0.08 dex and very small bias. In addition, weak AGNs that cannot be seen in the total spectrum may weakly bias (by 0.04 dex) the metallicity estimate that is derived from the galaxy-integrated spectrum.

Key words. galaxies: general – galaxies: abundances – supernovae: general

1. Introduction

Heavy elements up to the iron-groups are synthesized by fusion of lighter nuclei in the cores of stars. When the nuclear energy source in the core becomes exhausted, the star enters the final stage of its life. Within 4–40 Myr after their birth, stars heavier than ~8 $M_{\odot}$ form a heavy iron core that gravitationally collapses into a neutron star or a black hole (Bethe et al. 1979; Arnett et al. 1989), which in turn triggers an explosive ejection of the outer stellar envelope. This event is called a core-collapse supernova (CC SN). Stars with masses between 1.5 and 8 $M_{\odot}$ form a degenerate carbon-oxygen (C/O) white dwarf (WD; Becker & Iben 1980) with a mass in the range of 0.5−1.1 $M_{\odot}$ (Dominguez et al. 1999). If a C/O WD is in a binary system, it can accrete mass

from the companion stat (another WD, a main-sequence star, or a red giant star). Under certain conditions, the WD can increase its mass to ~1.4 $M_\odot$ and thermonuclear reactions can ignite in its center to completely disrupt the star in a very bright thermonuclear explosion (Hoyle & Fowler 1960) that is called a type Ia SN (SN Ia). This general picture is supported by the fact that CC SNe are only found in active star-forming galaxies, spiral arms, and H II regions (van Dyk 1992; Anderson et al. 2012; Galbany et al. 2014), which confirms that their progenitors probably are massive short-lived stars, while SNe Ia are found in all types of galaxies, including early-type galaxies without ongoing star formation.

Progenitor systems and the explosion mechanism of SNe Ia are still not fully understood, and no direct progenitor detection has been reported yet (but see McCully et al. 2014). However, there is growing evidence that the progenitor stars of SN Ia have wide range of ages following a delay-time distribution (DTD) with a form close to t^{-1} from hundreds of Myr to 11 Gyr (Maoz et al. 2010). It has been suggested that some small heterogeneities in the observed properties of SNe Ia can be attributed to differences in the mechanism that drives the explosion, such as the nature of the companion star (single- or double-degenerate scenario), or whether the explosion is initiated as a detonation or a deflagration.

Type II is the most common class of SN, and several progenitor stars have been detected in pre-explosion images, which has allowed constraining their initial mass to between 8.5 to 16.5 $M_\odot$ (Van Dyk et al. 2003; Smartt 2015). Although for the peculiar type II SN 1987A a blue supergiant (BSG) was suggested as a progenitor (Hillebrandt et al. 1987), the most viable candidates are red supergiants (RSG, Elias-Rosa et al. 2011; Maund et al. 2011). The more massive RSG probably result in type IIP (plateau or slow-decliners), and those that have lost large amounts of their H envelope and have yellow colors become type IIL SN (linear SN, or fast decliners). Type IIn SNe show narrow lines in their spectra, which result from interaction between the ejecta and circumstellar matter (CSM). For this reason, it has been proposed that their progenitors might be luminous blue variable (LBV) stars (Smith et al. 2008). Although only a few progenitor detections have been reported (Gal-Yam & Leonard 2009), there is evidence that SN IIn progenitors might be less massive than normal SN II (Anderson et al. 2012; Habergham et al. 2014).

Type Ibc SNe, also called stripped-envelope SNe, are less frequent, and fewer detections are available (see Liu et al. 2015). At the moment of explosion, SNe Ic have lost both their H and He layers and therefore show no H and He lines in their spectra. SNe Ib have lost only the outer H layer and show He lines. These explosions can occur through two possible channels. In the single-star scenario, the best candidates are massive (>25–30 $M_\odot$) Wolf-Rayet (WR) stars that have been stripped of their envelopes by strong line-driven winds, which are dependent on metallicity (Gaskell et al. 1986; Crowther 2007; Georgy et al. 2009). The other possibility is lower-mass stars that lose their outer envelopes during the evolution in a binary system (Podsiadlowski et al. 1992; Nomoto et al. 1996; Dessart et al. 2011). Although there should be a combination of the two scenarios, the binary scenario currently enjoys significant support (Fryer et al. 2007; Smith et al. 2011). A direct progenitor detection in pre-explosion images has been reported, but so far, it was not possible to constrain the exact nature of a progenitor system well (iPTF13bvn, Bersten et al. 2014; Eldridge et al. 2015). Finally, SNe IIb are a chameleon class between II and Ib. Initially, they show only hydrogen lines in their spectra, but at later stages helium lines appear as well. This suggests that SN IIb progenitors have retained only a thin layer of hydrogen on the surface. Possible detections of SN IIb progenitors and companions have been reported (SN 1993J, Aldering et al. 1994; Maund et al. 2004; SN 2011dh, Folatelli et al. 2014; Van Dyk et al. 2014), pointing to red (for SN 1993J) and yellow (for SN 2011dh) supergiants as the most likely candidates.

Because it is difficult to directly detect progenitors even in high-quality pre-explosion images, constraints on the possible scenarios that lead to different SN type explosions have been obtained through characterization of the SN environment (see Anderson et al. 2015, for a recent review). Of all the parameters that can be measured in the environment, the metallicity is of particular interest because it is expected to affect many aspects of the SN explosions, including the luminosity of SNe Ia and the type of CC SN that is produced by the massive stars (Bravo et al. 2010; Moreno-Raya et al. 2016; Modjaz et al. 2011). Most often, the observed SN properties have been correlated to the global metallicity of their host galaxies that were either directly measured or inferred from other proxies. Prieto et al. (2008), Kelly & Kirshner (2012), Prantzos & Boissier (2003), and Arcavi et al. (2010) all found that the number ratio of SN Ibc to SN II increases with metallicity. For SNe Ia, Childress et al. (2013) and Pan et al. (2014) found that the Hubble residuals correlated with the host gas-phase metallicity.

Several examples in the literature went further and tried to characterize the local properties of the SN environment. This is particularly relevant for the CC SNe, which explode closer to their birth place because their progenitors are short lived, and the metallicity measured at the SN location is assumed to be close to that of the progenitor. In contrast, the progenitor stars of SNe Ia most likely lived long enough to migrate around the galaxy, and the host galaxy properties at the SN explosion may not reflect the properties of the progenitor. Modjaz et al. (2008) found that SNe Ic with broad lines, which are associated with gamma ray bursts, come from host environments with a significantly lower metallicity than their counterpart SNe Ic. Using the radial position as a proxy for local metallicity, Anderson & James (2009) suggested a similar sequence in the progenitor metallicity of CC SNe. Anderson et al. (2010) and Leloudas et al. (2011) found no statistically significant difference between the local metallicity of SNe Ib and Ic, obtaining slit or fiber spectra at SNe positions. However, Modjaz et al. (2011) used local spectra and central spectra plus a metallicity gradient to claim that larger differences exist between SNe Ic and Ib. Taddia et al. (2013) studied the locations of SN1987A-like events whose progenitors are BSGs and found lower metallicities than for other CC SNe subtypes. Several studies tried to measure the local properties of the SN environment for SNe Ia by either using the offset as a proxy for these local properties (Galbany et al. 2012) or by indirect approximations of the central metallicity and by applying decreasing gradients (Boissier & Prantzos 2009).

In this series of papers (Stanishev et al. 2012 and Galbany et al. 2014, hereafter Paper I) we take a different approach. We used wide-field integral field spectroscopy (IFS) at the intermediate spectral resolution provided by the CALIFA survey (Sánchez et al. 2012a) combined with other previous observations to measure the properties of the gas and the stellar populations at the location of the SN explosion (in addition to other global host properties). Our goal is to search for differences in environmental parameters of SN types, which would also help in constraining the nature of their progenitors. We also tested the accuracy of the various proxies to the local metallicity used in

Table 1. Properties of the 37 SNe added to the sample presented in Paper I.

Galaxy	Morphology	z	$E(B-V)$	PA [deg]	b/a	*SN*	Type	RA offset [arcsec]	Dec offset [arcsec]	Separation [arcsec]
UGC 04132	Sbc	0.017409	0.067	116.7	0.42	2014ee	IIn	−17.1	−14.0	24.9
NGC 5406	SAB(rs)bc	0.017352	0.011	17.9	0.94	PSN J14002117+3854517	II	+5.0	+3.0	4.9
NGC 6166	cD2 pec	0.030354	0.012	123.8	0.95	PS15aot	Ia-91bg	+1.5	−8.6	8.5
NGC 0309	SAB(r)c	0.018886	0.035	26.8	0.93	1999ge	II	+16.0	+6.7	17.6
NGC 0938	E	0.013736	0.100	91.9	0.77	2015ab	Ia	−9.3	+6.3	11.7
NGC 0991	SAB(rs)c	0.005110	0.024	36.7	0.94	1984L	Ib	−32.0	−22.0	35.0
UGC 02134	Sb	0.015297	0.151	8.2	0.51	2011jf	Ibc	+3.0	−1.0	37.2
NGC 1070	Sb	0.013636	0.050	89.8	0.75	2008ie	IIb	-22.0	+13.0	25.4
MCG -01-09-006[†]	SB(rs)cd?	0.028977	0.066	107.5	0.32	2005eq	Ia	+15.9	+26.3	30.3
IC 0307[†]	(R)SB(r)a pec?	0.025981	0.086	149.1	0.61	2005em	IIb	+38.0	-7.9	38.3
MCG -01-10-019[†]	SAB(r)cd	0.017505	0.050	105.7	0.72	2001H	II	+5.8	−2.9	4.6
NGC 1667	SAB(r)c	0.015167	0.067	77.8	0.65	1986N	Ia	−12.0	−9.0	19.6
UGC 04195	SB(r)b	0.016305	0.050	111.0	0.71	2000ce	Ia	+15.1	+17.3	22.6
NGC 2554	S0/a	0.013870	0.050	70.0	0.77	2013gq	Ia	−0.6	−9.1	9.2
NGC 2565[†]	(R')SBbc?	0.011948	0.042	81.1	0.50	1992I	II	−28.5	+7.1	28.9
						1960M	I	−13.0	+34.0	37.6
NGC 2577[†]	S0	0.00678	0.048	16.8	0.51	2007ax	Ia	−2.6	+5.5	6.4
NGC 2595	SAB(rs)c	0.014443	0.035	125.9	0.95	1999aa	Ia	+1.0	+28.0	30.0
NGC 2596	Sb	0.019807	0.037	158.1	0.40	2003bp	Ib	+17.6	+11.6	22.0
NGC 2604	SB(rs)cd	0.006930	0.041	52.4	0.96	2002ce	II	−16.0	−12.0	23.1
UGC 04468	S0	0.025227	0.030	74.0	0.34	2006bb	Ia	+3.6	−27.5	27.7
NGC 2916	SA(rs)b?	0.012442	0.023	105.8	0.63	1998ar	II	+16.9	+38.5	42.3
UGC 05520	Scd	0.011058	0.034	15.0	0.63	2000L	II	+6.9	−19.3	22.0
NGC 5425[†]	Sd	0.006918	0.018	38.5	0.35	2011ck	IIP	−14.8	+7.3	16.1
NGC 5525	S0	0.018523	0.022	109.1	0.36	2009gf	Ia	−31.0	−8.5	32.0
NGC 5557[†]	E1	0.010737	0.006	120.3	0.94	1996aa	Ia	−5.0	+3.0	4.2
NGC 5559[†]	SBd	0.017232	0.020	152.1	0.33	2001co	Ibc−pec	−13.5	−12.6	18.4
NGC 5587[†]	S0/a	0.007682	0.023	73.1	0.32	2006dy	Ia	+10.0	+9.0	14.1
NGC 5732	Sbc	0.012502	0.015	130.4	0.56	ASASSN-14jf	II	+8.2	−17.6	20.0
NGC 6063	Scd?	0.00950	0.041	62.5	0.56	1999ac	Ia−pec	+23.9	−29.8	38.3
UGC 10123	Sab	0.012575	0.013	147.5	0.36	2014cv	IIP	+8.0	+2.0	6.0
NGC 7619	E	0.012549	0.072	116.5	0.85	1970J	Ia	−27.0	−30.0	37.0
NGC 7691	SAB(rs)bc	0.013479	0.062	79.1	0.98	2014az	IIP	−22.0	+18.0	28.4
UGC 06517	Sbc	0.008309	0.029	124.2	0.72	2006lv	Ibc	+10.0	+12.0	15.3
IC 0758	SB(rs)cd?	0.004253	0.018	109.8	0.93	1999bg	IIP	−33.0	−20.0	36.6
UGC 09356[†]	S?	0.007419	0.027	15.2	0.46	2011cj	IIP	+4.4	+7.5	8.2
2MFGC 13321	Sb	0.026145	0.007	168.6	0.39	2002aw	Ia	−1.6	+1.5	3.4

Notes. This corresponds to 34 SNe in 33 galaxies observed from June 2014, and 3 SNe that recently exploded in NGC 5404, NGC 6166 and UGC 04132. The morphological galaxy type, redshift, Milky Way dust reddening, and SN angular separation are from the NED database. SN type and offset (positive in the N and E direction) obtained from the Asiago SN catalogue. The position angle (PA, W to N) and the axis ratio (b/a) are calculated in this work. [(†)] Only observed with the V500 grating.

the literature. Kuncarayakti et al. (2013a,b, 2015) also used IFS observations, but with a smaller field of view that covered only a small part of the galaxies.

In this second paper of the series we focus on the local SN metallicity. The paper is structured a follows. The galaxy sample of SN hosts used in this work is presented in Sect. 2. The methods used to extract the necessary information for this study from the observed IFS data-cubes is outlined in Sect. 3. We present our results in Sect. 4. Section 5 contains the discussion of these results, and we summarize the conclusions in Sect. 6.

2. Galaxy and supernova samples

The galaxy and SN selection has been described in Paper I, and more details, including the data reduction, can be found there. We here expand the sample presented in Paper I with 33 galaxies (the details are given in Table 1) that hosted 34 discovered SNe. In addition, 3 new SNe exploded in two galaxies that were presented in Paper I. The total sample used in this work therefore consists of 115 galaxies with a mean redshift of 0.015, which hosted 132 SNe (47 type II SNe, 27 type Ib/c+IIb SNe, 58 Ia SNe) that were in the FoV of PPAK. Eighty-one galaxies were observed by the CALIFA survey and 34 fby other CALIFA-related studies that used the same instrumental configuration. Twelve of the 79 galaxies from CALIFA were delivered to the community in the CALIFA Data Release 1 (DR1, Husemann et al. 2013) and 12 more in the CALIFA DR2 (García-Benito et al. 2015). Table 2 gives the mean and the standard deviation of the redshift distributions of the whole sample, split by SN type.

Seven galaxies of the sample (NGC 214, NGC 309, NGC 628, NGC 1058, NGC 3184, NGC 3913 and NGC 5557)

Table 2. Statistics of the redshift distributions.

	Ia	Ibc/IIb	II	All
$\langle z \rangle$	0.0179	0.0125	0.0128	0.0150
σ_z	0.0090	0.0063	0.0074	0.0083

	II – Ibc/IIb	II – Ia	Ibc/IIb – Ia	CC – Ia
KS test	0.991	0.051	0.063	0.019
($z < 0.02$)	0.951	0.120	0.189	0.087

Table 3. Statistics of the SNe.

	II	Ibc/IIb	Ia		All
			SF	P	
SNe in CALIFA hosts	54	32	59	15	160
Inside the PPAK FoV	47	27	46	12	132

Notes. SNe Ia in star-forming (SF) and passive (P) hosts are given separately.

also hosted ten SNe that were outside of the FoV of PPAK. Another 18 galaxies from the CALIFA sample have SNe associated with them (one SN in each galaxy), but these SNe are outside of the FoV[1]. These SNe were only used to check the analysis results of the total galaxy properties of the main sample. We found that adding these extra SNe to the main sample did not change the results. The parameters of these 25 galaxies with SNe outside the FoV are given in Table D.1. In Table 3 the number of SNe in the galaxies in our sample grouped by SN subtype is summarized.

Almost all SNe in our sample were discovered by targeted searches. It is known that these searches are biased toward more massive galaxies than are untargeted surveys. As we show in Sect. 5.1, most galaxies in our sample indeed have masses higher than $\log(M/M_\odot) \simeq 10$. This means that the results presented in this work are representative for SNe discovered in targeted searches.

The 3D data cubes used in this work, including those presented in Paper I, were processed with version 1.5 of the CALIFA reduction pipeline (García-Benito et al. 2015). Nine of the galaxies of Paper I that at the time were observed only with the red V500 grating (spectral resolution ~6 Å and coverage within 3750–7300 Å) have now also been observed with the blue V1200 grating (spectral resolution ~2.7 Å and coverage within 3400–4750 Å). For these objects the combined V1200 + V500 data cubes were used.

3. Data analysis

The data analysis has been fully described in Stanishev et al. (2012) and Paper I. Here we summarize the main steps and add those that were not included in the previous papers. We note that the measurements presented here and in Paper I are independent of the data analysis method used, and a comparison of several methods within the CALIFA collaboration will be matter of a future work (Rosales-Ortega et al. in prep.)

Each galaxy data cube consists of approximately 4000 spectra spread in square spaxels of $1'' \times 1''$ in a hexagonal FoV of 1.3 arcmin^2. We applied our analysis procedures to all the individual spectra. For most galaxies the spectra in the outer parts have a signal-to-noise ratio (S/N) that is insufficient to extract useful information. To analyze the 2D maps of these galaxies, spatial binning was applied using adaptive Voronoi tessellations (Cappellari & Copin 2003; Diehl & Statler 2006). The new combined spaxels were required to have a S/N of around 20 in the continuum band at 4610 ± 30 Å.

The main goal of this paper is to study the metallicity at the SN locations, both stellar and gas-phase metallicity. However, in many cases the SN location is located on a spaxel with a low S/N. Because the Vironoi binning is an automatic procedure, the new bins are generally not centered on the SN locations. To measure the metallicity at the SN location, we followed the same approach as in Paper I. Series of spectra were extracted in apertures centered on the SN positions. The apertures had radii of up to 6″. For some SNe even this was not enough to measure the stellar metallicity, and in a few cases the gas metallicity could likewise not be measured[2]. The aperture of the spectrum of each SN used for the analysis in this work is given in Tables D.2 to D.4.

We also analyzed the total galaxy spectra formed by simply summing the individual spaxel spectra with $S/N \geq 1$. This removed the outer low S/N part of the FoV, which contains little light from the galaxy and mostly adds noise to the summed spectrum. In several cases, foreground stars in the FoV were also masked out. This analysis was performed to compare the properties of the host as derived from integrated spectroscopy to those derived from spatially resolved spectroscopy.

To measure the emission lines flux accurately, the stellar continuum was subtracted using `STARLIGHT` (Cid Fernandes et al. 2005). We performed series of tests comparing the base of 66 single stellar population (SSP) models with different ages and metallicities from Stanishev et al. (2012) and Paper I, extracted from the Charlot & Bruzual 2007 models (Bruzual 2007), with another basis consisting of 260 SSPs from the basis described in González Delgado et al. (2014). The latter covers ages from 1 Myr to 18 Gyr, four metallicities – 0.2, 0.4, 1.0, and 1.66 $Z_\odot$, where $Z_\odot = 0.019$, and uses a Salpeter (1955) initial mass function (IMF). We found that the choice of basis has little effect on the measured emission line fluxes. To speed up the analysis, we therefore used the 66 SSPs basis for the continuum subtraction and measurement of the gas-phase properties. The most prominent emission lines were fit using a weighted nonlinear least-squares fit with a single Gaussian plus a linear term, and corrected for dust attenuation using the ratio of Hα and Hβ emission line fluxes. Finally, spatially resolved 2D maps of the flux and error for each line were produced.

For the analysis of the properties of the stellar populations, our test indicated that the properties recovered with the larger basis were more stable. In particular, the stellar metallicity showed smaller scatter in a given galaxy. The estimates of the stellar mass from the total spectra and the stellar age and metallicity for each particular measurement were therefore obtained from the `STARLIGHT` fits with the 260 SSPs basis. We here focus on the mass-weighted metallicity estimate. To calculate the galaxy masses, the distances inferred from the Hubble law were used. Only for the very nearby galaxies we used distances from the Cepheid, Tully-Fisher, or another direct method when available.

[1] We detected up to twelve supernovae in our galaxy sample that lack from spectroscopic classification. We have not considered them anywhere in this analysis.

[2] Even though metallicity is derived from the spectra at the SN spaxel with $1 \times 1''$ size, the resolution of the cubes is ~2.57". The effect of this is discussed in detail in Sect 5.2.

3.1. Oxygen abundance

Nebular emission lines are a good tracer of the young and massive stellar populations that ionize the interstellar medium (ISM), and they are the main tool at our disposal for the direct measurement of the metal abundance. Since oxygen is the most abundant metal in the gas phase and exhibits very strong nebular lines in optical wavelengths, it is commonly chosen as a metallicity indicator in ISM studies. The most accurate method to measure ISM abundances (the so-called direct method) involves determining the ionized gas electron temperature, T_e, which is usually estimated from the flux ratios of auroral to nebular emission lines (e.g., [O III] $\lambda\lambda$4959, 5007/[O III] λ4363, Izotov et al. 2006; Stasińska 2006). However, temperature-sensitive lines such as [O III] λ4363 are very weak and difficult to measure, especially in metal-rich environments. Using V1200 CALIFA data for 150 galaxies, Marino et al. (2013, M13 hereafter) identified only 16 H II regions in which this line can be measured and used them to reliably derive T_e. Because it is difficult to find the correct emission lines from which to estimate the metallicity with the direct method, alternatives have been developed over the years. The so-called empirical methods consist of a combination of easily measurable gas emission parameters that are calibrated against the metallicities previously determined by the direct method from H II regions and galaxies. In constrast, theoretical methods are calibrated by comparing the measured line fluxes with those predicted by theoretical photoionization models. While these two methods have been proved to be sensitive to relative variations of the metallicity, they also showed systematic differences on the absolute metallicity scale (see Kewley & Ellison 2008 for a review). Theoretical methods have been shown to overestimate the metallicity by a few tenths of dex, and empirical methods may underestimate it (Moustakas et al. 2010). Since our aim is to determine the gas oxygen abundances at SN sites within the galaxies and the direct method cannot be used everywhere reliably with our data, we used several of the alternative methods described above.

As a primary method, we used the empirical calibration based on the O3N2 index, first introduced by Alloin et al. (1979), which gives an estimation of the oxygen abundance based on the difference of the O3 and N2 line ratios. This calibration has the advantage of being insensitive to extinction because the separation in wavelength of the emission lines used for the ratio diagnostics is small and does not suffer from differential atmospheric refraction (DAR). The extinction is not a problem in our case since our emission line measurements are already extinction corrected. Recently, M13 presented new calibrations for this O3N2 and for the N2 indices that include new direct abundance measurements at the high-metallicity regime, which is an advantage over the most frequently used Pettini & Pagel 2004 (hereafter PP04) calibration of O3N2 that used photoionization models for this regime instead. Although the relative differences between the two calibrations are kept, these new calibrations give more physical results and do not allow very high values of the oxygen abundance (e.g. >9.0 dex), for example. For this reason, the main analysis was made using the empirical calibration introduced in M13.

We used three different methods to check the O3N2 results: (a) the M13 calibration based only on the N2 index; (b) the method described in Pilyugin et al. 2010 (hereafter P10), which makes use of the [O II] $\lambda\lambda$3726, 3729 doublet; and (c) the method described in Pilyugin & Mattsson 2011 (hereafter P11), which uses the [S II] doublet.

We note that the emission line measurements that fall in the AGN region in the BPT diagram (Baldwin et al. 1981) according to the Kewley et al. (2001) criterion were excluded from the analysis throughout the paper. This was mainly the case in the central spaxels of a significant fraction (~50%) of our galaxies.

3.2. Metallicity gradients

The radial variation of the metal abundance in galaxies has been studied in several works using a wide range of approaches and instruments (Diaz 1989; Zaritsky et al. 1994; Garnett et al. 1997; Henry & Worthey 1999; Rolleston et al. 2000; Boissier & Prantzos 2009; Sánchez et al. 2012b; Marino et al. 2016). It is now commonly accepted that the radial metallicity decreases toward the galaxy outskirts. This can be explained by the combined effects of a radially varying star formation rate and gas in-fall. It has also been suggested that the magnitude of the radial decrease has a characteristic value (Diaz 1989; Vila-Costas & Edmunds 1992; Bresolin et al. 2009; Yoachim et al. 2010; Rosales-Ortega et al. 2011). IFS is the best-suited technique to study the metal abundance distribution across the galaxy surface in detail and gain insight on its radial dependence. Using HII regions of about 300 galaxies observed by CALIFA Sánchez et al. (2014) have demonstrated the universality of the gradient, which has been confirmed by Sánchez-Menguiano et al. (2016) through a spaxel by spaxel analysis.

We determined metallicity gradients in our galaxy sample using our method for estimating the disk effective radius (see Appendix A) as well as the galaxy position angle and inclination. For each galaxy the metallicity obtained at each spaxel was plotted as a function of the deprojected galactocentric distance and fit with a first-order polynomial to estimate the galaxy metallicity gradient. As stated in Sect. 3.1, the central spaxels that showed emission from AGN were removed from the fit because the gas emission lines observed in these regions are not caused by ionization from young massive stars. All the 11 passive or elliptical galaxies in our sample show weak emission in their central regions, which in all cases was classified as coming from an AGN. Five of these galaxies also showed traces of weak emission lines in the central parts outside the AGN-affected region, but these were not strong enough to measure gradients.

In most galaxies the metallicity decreases with the radial distance. A clear example of the general case is given in Fig. 1 (top panel) for NGC 4961. However, in some galaxies a metallicity decrease or flattening close to the center was found (see UGC 03555 in Fig. 1 bottom panel). This central metallicity decrease was first noted by Rosales-Ortega et al. (2011) and Sánchez et al. (2012b) and was studied in more detail with the whole CALIFA sample by Sánchez et al. (2014), who found that about 25% of the galaxies showed the decrease. This feature appears to be associated with a circumnuclear star formation ring, where gas tends to accumulate as a result of non-circular motions (Fathi et al. 2007) and does not seem to be associated with the morphological type of galaxies or with the presence of a bar. In our sample, 18 out of 58 (31%) of the SN Ia, 13 out of 47 (28%) of the SN II, and 7 out of 27 (26%) of the SN Ibc host galaxies showed the central decrease. When we include those galaxies that show a flattening instead of a decrease toward the center, all percentages increase to around 40%. It is also interesting to note that ~50% of the galaxies hosting an AGN (27 out of 58) show the central metallicity decrease, while when the 11 elliptical galaxies are excluded, the percentage increases to ~60% (27 out of 47). In addition, 30% (8 out of 27) of the galaxies that fall

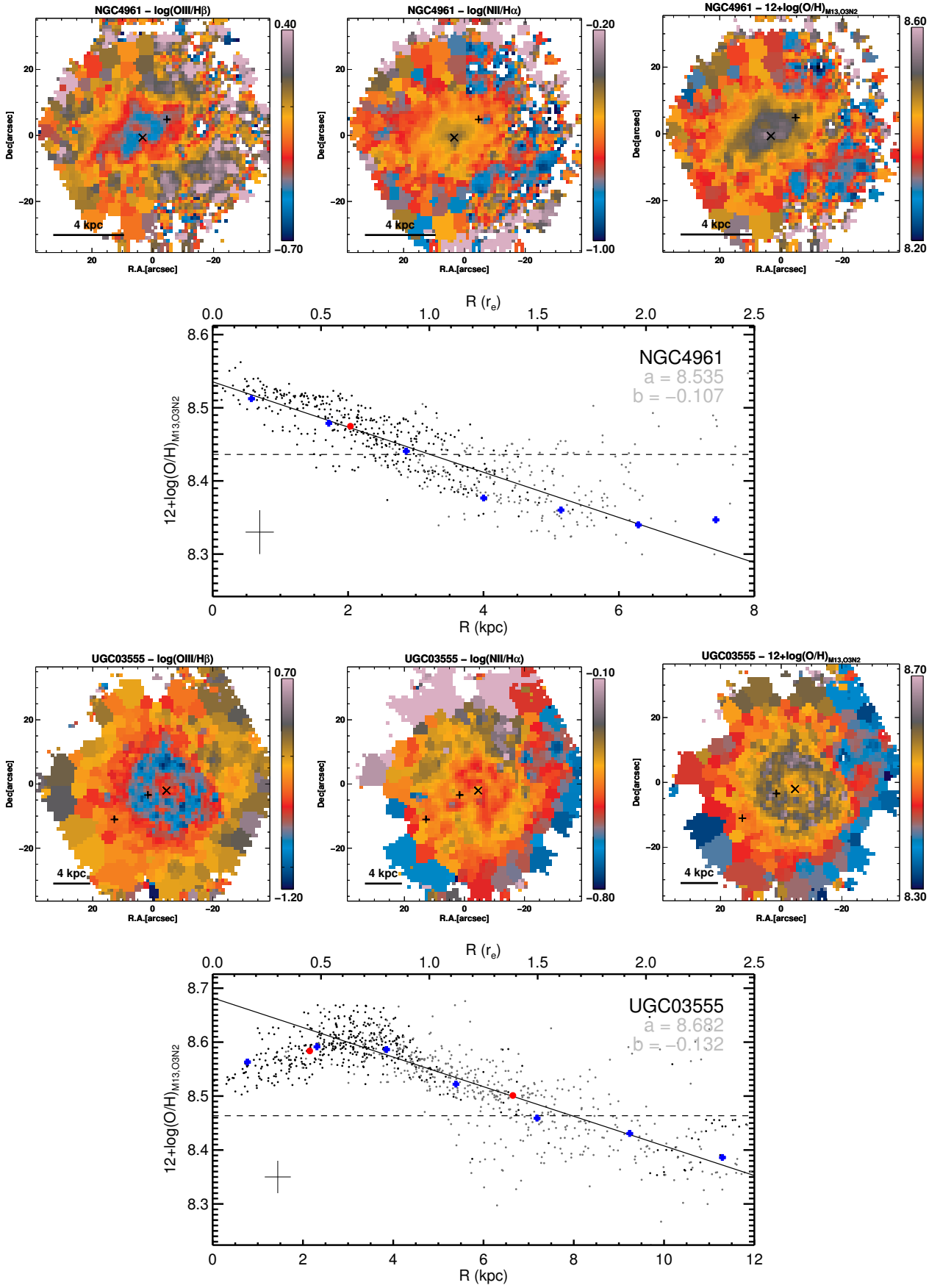

Fig. 1. NGC 4961 and UGC 03555 OIII/Hβ, NII/Hα, and oxygen abundance maps (*top*) and gradient fits (*bottom*). Black dots show measurements in individual spaxels, gray dots measurements in Voronoi spaxels, blue dots measurements from azimuthal averaged spectra, and red dots represent measurements from the spaxels where SNe exploded (2001ee-II in the *top panel*, and 2004ge-Ic/1999ed-II in the *bottom panel*). Mean representative *X*- and *Y*- errors are plotted in the lower left corner for reference.

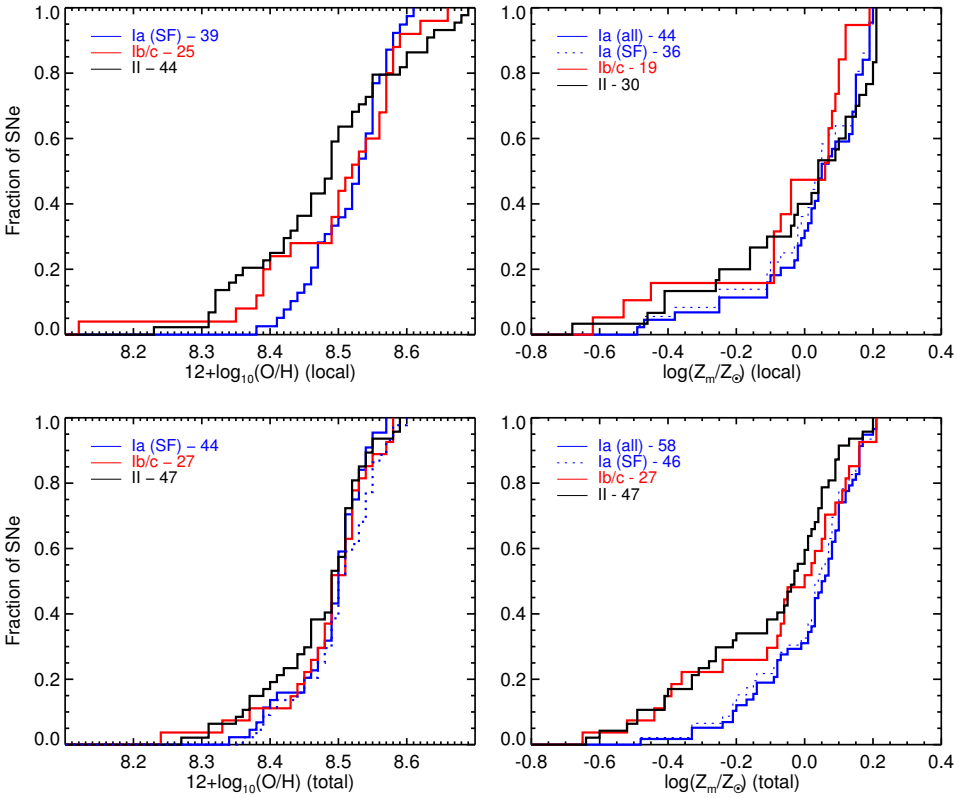

Fig. 2. SN environment measurements of the oxygen abundance (*left*) and the mass-weighted stellar metallicity (*right*) for galaxies hosting different SN types. In the *top row* we show the distributions of the local metallicity, while in the *bottom row* total metallicity distributions are plotted. The ordinate indicates the fraction of the SN population with metallicities lower than the abscissa value.

in the composite region of the BPT diagram also show the decrease, but only one of those located in the star-forming region (UGC 03555) shows this effect. Exploring the possible connection between the central metallicity decrease and the presence of AGN is certainly interesting, but it is beyond the scope of this paper.

4. Results

In this section we explore the 2D maps of SN host galaxies in search for correlations between the SN type and the properties of their host galaxies regarding the gas elemental abundance and the stellar metallicity. There are 11 galaxies (hosts of 12 SNe Ia) in our sample that after subtracting the stellar continuum contribution do not show emission lines at any position or only show weak emission in their central regions: NGC 0495, NGC 1060, NGC 2577, UGC 04468, NGC 4874, NGC 5557, NGC 5611, UGC 10097, NGC 6166, NGC 6173, and NGC 7619. As in Paper I, we used these 12 SNe Ia only when the parameter needed for the analysis is measurable. In the following sections most of the results are presented in the form of cumulative distributions (CDFs). We performed tests to determine whether the differences between the mean values and the standard deviations of the distributions were statistically significant. Two-sample Kolmgorov-Smirnov (KS) tests were also performed to verify that the data were drawn from the same underlying population. The measured quantities for individual galaxies and SNe are reported in Tables D.2–D.4. In Tables 4–7 we give the mean and median statistics of the distributions and their asymmetric errors for the three SN subtypes.

4.1. Global and local metallicities

The cumulative distributions of the local gas and stellar metallicities for each SN type are shown in the upper row of Fig. 2, and the properties of the distributions are given in Table 4. There are differences between the distributions of the local gas-phase metallicity among the SN types, but the KS test indicates that only the distribution of SN Ia and SN II might be different at 95% significance. The differences between the mean total metallicities are also small (~0.04 dex), and the statistical tests again indicate that the differences might be significant only between SN Ia and SN II at 95% significance. It is also interesting that the standard deviation of the distribution for SNe Ia is twice as small as those of the core-collapse SNe, and this difference appears to be statistically significant. The differences between the mean stellar metallicitiy at the SN location are larger than for the gas-phase metallicity, but the standard deviations of the distributions are also significantly larger. The KS test indicates no statistically significant differences between the distributions. Even though the differences between the mean metallicities at the SN locations are small, it is worth noting that SN Ia have the highest metallicity of the three SN types.

The lower row of Fig. 2 shows the cumulative distributions of the total galaxy metallicity. The gas-phase metallicity of the three SN types hosts is on average very similar for the three SN types (~8.48 dex), and the distributions are statistically indistinguishable. However, similarly to the metallicity at the SN locations, the standard deviation of the distribution of SNe Ia hosts is smaller than that of the core-collapse SNe. The total stellar metallicity shows noticeably larger differences between the three SN types, with the difference between SN Ia and SN II being statistically significant. Again, even tough the differences are small, SN Ia have the highest metallicity of the three SN types.

Figure 3 shows the cumulative distributions of the difference between the local and the global metallicity. The properties of the distributions are given in Table 5. All distributions are centered on a location close to zero, but there are small differences between the SN types. The local gas-phase metallicity of SN Ia is on average 0.03 dex higher than the total galaxy metallicity,

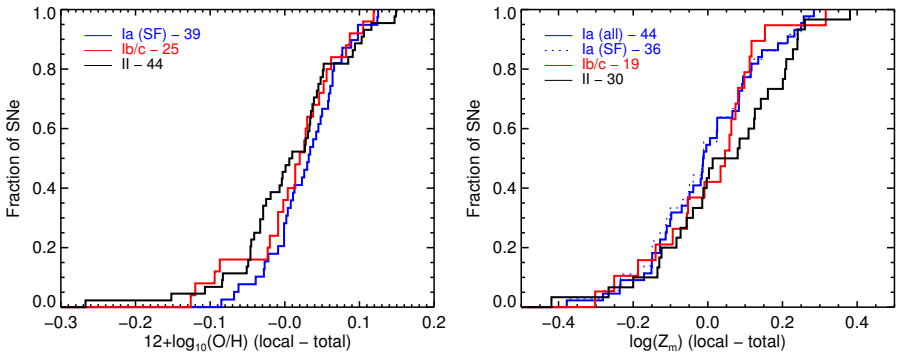

Fig. 3. Differences between the local and the total oxygen abundance (*left*) and mass-weighted stellar metallicity (*right*) for different SN types.

Table 4. Properties of the distributions of the gas-phase and stellar metallicities at the SN location and the total galaxy.

SN type	Mean	σ	σ_m	Median	N
		$12+\log(\mathrm{O/H})_{\mathrm{local}}$			
Ia	8.522	0.056	0.009	8.537	39
Ib/c	8.500	0.114	0.023	8.520	25
II	8.484	0.112	0.017	8.494	44
		$12+\log(\mathrm{O/H})_{\mathrm{total}}$			
Ia	8.492	0.054	0.008	8.505	44
Ib/c	8.489	0.076	0.015	8.500	27
II	8.477	0.074	0.011	8.500	47
		$\log(Z_m/Z_\odot)_{\mathrm{local}}$			
Ia	0.032	0.173	0.026	0.052	44
Ib/c	−0.049	0.232	0.053	0.067	19
II	−0.012	0.238	0.043	0.043	30
		$\log(Z_m/Z_\odot)_{\mathrm{total}}$			
Ia	0.021	0.149	0.020	0.060	58
Ib/c	−0.069	0.239	0.046	0.007	27
II	−0.105	0.223	0.033	−0.022	47

Notes. Shown are the mean, the standard deviation σ, the standard deviation of the mean σ_m, the median, and the number of SNe.

and this is the only difference that is statistically significant. The differences between the local and the global stellar metallicities is not significant for any SN type.

4.2. Other proxies of the local metallicity

In the past several indirect measurements have been used to estimate the metallicity at the SN location. The spatially resolved spectroscopy nature of our data allowed us to estimate the metallicity at the SN position and at the same time to compare it to the metallicity at the SN location estimated by other approximations. Therefore, we are in a position to test whether these methods are good proxies for the local SN metallicity.

In the previous section we have shown that the metallicity measured from the total galaxy spectrum is a fair approximation of the local metallicity. In this section we focus on several other proxies. The results of these proxies are given in Table 5 for the three SN types and are explained below.

4.2.1. Central metallicity

The Sloan Digital Sky Survey and other galaxy surveys use fiber spectrographs to provide thousands of spectra of the central regions of galaxies in the nearby Universe. Such surveys can be very useful for SN studies (see, e.g., Prieto et al. 2008), but this

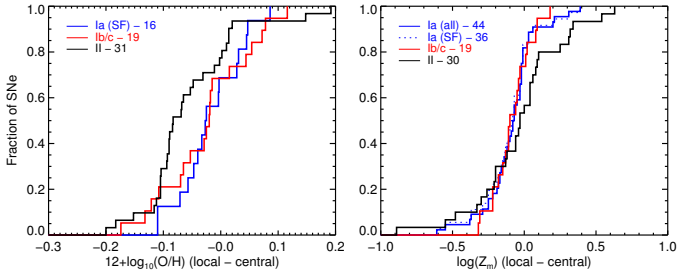

Fig. 4. Distributions of the differences between local and central metallicity.

approach has several drawbacks. Galaxies with AGN cannot be used because the strong-line methods for gas-phase metallicity estimate are no longer valid. As we discuss in Appendix A, a large fraction of the galaxies in our sample have AGNs. More specifically, 59% of the star-forming SN Ia hosts (27 of the 46), 22% of SN Ibc/IIb hosts (6 out of 27) and 32% of SN II hosts (15 out of the 47) have AGNs. As we have already shown in Paper I, there is a higher ratio of SN Ia host galaxies that have an AGN compared to the galaxies that hosted other SN types. This ratio would increase to 67% if the 11 elliptical galaxies, all of which host an AGN, were included.

Figure 4 shows the distribution of the differences between the local metallicity and the metallicity measured at the galaxy core only for those galaxies for which both measurements are available. For the gas-phase metallicity all distributions have negative mean values, and thus the central metallicity is an overestimation of the metallicity at the SN position. The offsets are small, −0.018, −0.025, and −0.055 dex for SN Ia, Ibc, and II, respectively, and only the offset for SN II is statistically significant. The smallest offset for SNe Ia could be explained by the metallicity decrease toward the center in some galaxies (see previous section). More than half of SN Ia hosts in our sample have such a decrease, which would center the distribution toward zero. The fraction of galaxies with the central decrease among the CC SN hosts is lower and hence the offset is larger. The differences of the stellar metallicities are −0.088, −0.083, and −0.030 dex for SN Ia, Ibc, and II, respectively; only the first two are statistically significant. The corresponding standard deviations are $\sigma_{\mathrm{Ia}} = 0.19$, $\sigma_{\mathrm{Ibc}} = 0.13$, and $\sigma_{\mathrm{II}} = 0.32$ dex. These results indicate the error that arises when the central metallicity is used as a proxy for the local metallicity. However, because the standard deviation and the offset from zero are both larger than that for the total metallicity, its accuracy is lower.

Our findings agree with those of Modjaz et al. (2011), who found that local metallicities of SN Ibc in their sample were generally lower than central metallicities. However, their central estimate was derived from the host galaxy luminosity and not from gas emission line ratios. Our results also agree with

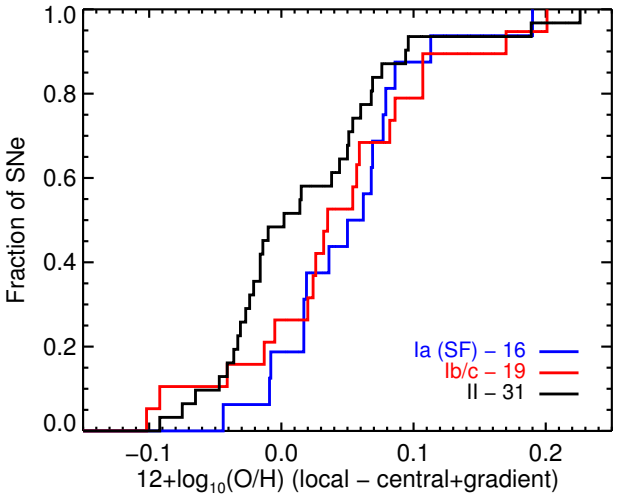

Fig. 5. Distribution of differences between local metallicity and the proxy using the central metallicity plus a characteristic gradient.

Sanders et al. (2012), who claimed that central and local metallicities are equal within 0.1 dex (in PP04 scale).

4.2.2. Central metallicity plus characteristic metallicity gradient

Another approach for estimating the local metallicity is to use the central metallicty plus the characteristic metallicity gradient (in normalized units). This can be very useful for galaxy surveys that were performed with multifiber spectrographs like SDSS, which for low-redshift galaxies only provide the central metallicity. We here normalized the individual metallicity gradients to a common ruler, the disk effective radius r_e, which contains half of the total integrated flux from the disk component. The procedure followed to estimate r_e is described in Appendix A. We have tested this approach, and Fig. 5 shows CDFs of the differences. Of all proxies considered here, this one shows the largest mean differences and appears to be the least accurate (Table 5). Only the difference for SN II is not statistically significant. The larger offset for SN Ia is likely due to the larger fraction of hosts with central metallicity decrease, which will bias this estimator.

4.2.3. Metallicity gradient and radial distance

Metallicity gradients measured with long-slit spectroscopy have been used to estimate the metallicity at the location of SN explosions. The gradients are typically measured by placing the slit along the galaxy major axis, and then the metallicity at the radial distance of the SN is estimated. We estimated the gas-phase metallicity at the SN location using the individual metallicity gradient for each galaxy obtained in Sect. 3.2 and the deprojected GCD of the SN. In the left panel of Fig. 6 we show the distributions of the differences between the metallicity at the SN position and that estimated using the gradients. We see that all SN types have narrow distributions with standard deviations of $\sigma_{Ia} = 0.085$, $\sigma_{Ibc} = 0.053$, and $\sigma_{II} = 0.071$ dex, and no significant differences in the average values can be seen for different SN types. This is an indication that a (well-measured) metallicity gradient could be a good approximation to the value at SN position for SNe Ibc and II. For SN Ia the total metallicity appears to be a better approximation.

Table 5. Distribution properties of the differences between the metallicity estimated from local measurements and the metallicity estimated using different proxies.

SN type	Mean	σ	σ_m	Median	N
		$12+\log(O/H)_{local-total}$			
Ia[a]	0.029	0.050	0.008	0.032	39
Ib/c	0.012	0.064	0.013	0.020	25
II	0.006	0.078	0.012	0.008	44
		$12+\log(O/H)_{local-H\,II}$			
Ia	−0.004	0.035	0.006	0.001	39
Ib/c	0.007	0.037	0.007	−0.001	25
II	0.008	0.042	0.006	0.002	42
		$12+\log(O/H)_{local-gradient}$			
Ia	−0.014	0.045	0.007	−0.007	39
Ib/c	−0.003	0.041	0.008	−0.002	25
II	0.001	0.069	0.011	0.005	43
		$12+\log(O/H)_{local-central}$			
Ia	−0.018	0.056	0.014	−0.026	16
Ib/c	−0.024	0.077	0.018	−0.019	19
II[a]	−0.056	0.082	0.015	−0.082	31
		$12+\log(O/H)_{local-central+gradient}$			
Ia[a]	0.052	0.056	0.014	0.057	16
Ib/c[a]	0.043	0.077	0.018	0.036	19
II	0.020	0.071	0.013	0.003	31
		$\log(Z_m)_{local-total}$			
Ia	−0.004	0.150	0.023	−0.011	44
Ib/c	0.004	0.150	0.034	0.047	19
II	0.042	0.178	0.032	0.047	30
		$\log(Z_m)_{local-central}$			
Ia[a]	−0.086	0.185	0.028	−0.070	44
Ib/c[a]	−0.083	0.131	0.030	−0.099	19
II	−0.029	0.311	0.057	−0.024	30

Notes. Shown are the mean, the standard deviation σ, the standard deviation of the mean σ_m, the median and the number of SNe. [(a)] statistically significant difference.

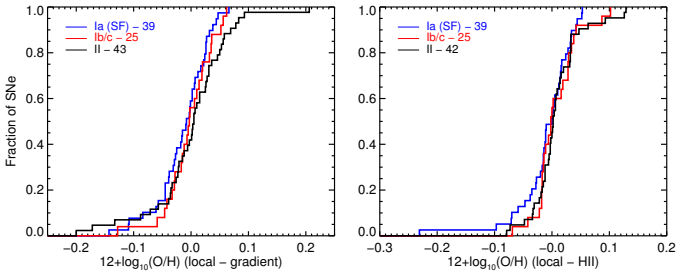

Fig. 6. Distribution of differences between local metallicity and the proxy using gradients (*left*) and the metallicity of the closest HII region (*right*). All measurements performed with O3N2 index.

4.2.4. Closest HII region

As in Paper I, HIIEXPLORER (Sánchez et al. 2012b) was used to extract HII regions from the extinction-corrected Hα emission maps. The caveats of this method are fully described in Paper I, but we recall that the main drawbacks are that (i) we select clumps of HII regions (1 to 6, Mast et al. 2014) instead of individual regions, especially in more distant galaxies; and (ii) this

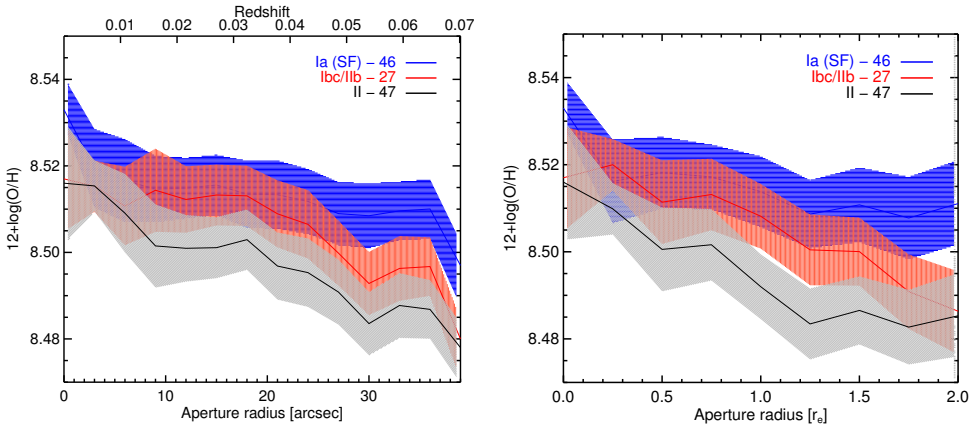

Fig. 7. *Left*: mean values for oxygen abundance from the central spaxel (value at 0 arcsec) to the total spectra (value at 39 arcsec), increasing the aperture in steps of 3 arcsec. Error bands are errors of the mean values. The upper x-axis shows where the aperture with 3″ diameter is projected for different redshifts. *Right*: same measurements, but normalizing the unit of the aperture to the effective radius of the galaxies.

method tends to select regions with similar sizes, although this is not the case of real H II regions in galaxies.

For each SN, we determined the SN host H II region by selecting the clump that is closest to the SN location in terms of deprojected distance. The spectra of the spaxels belonging to that H II region were co-added and analyzed. It is reasonable to consider that for CC SNe the progenitor might be formed in fainter H II regions that are not detected by this method. For SNe Ia it is difficult to associate the selected H II region because the place where the progenitor was formed as SNe Ia may have old progenitors, which might have migrated from their birthplace.

In the right panel of Fig. 6 we show the distributions of the differences among the metallicity at the SN position and that of the closest H II region. All distributions are centered on zero within 0.01 dex and have small standard deviations ~0.04 dex[3]. The standard deviations are smaller than both the local metallicity estimates using gradients and the total metallicity, which means that the metallicity of the nearest H II region is a better approximation. This is expected because compared to the other proxies of the local metallicity, the nearest H II region is the most direct measurement.

4.3. Aperture effects

At low redshift fiber spectrographs usually measure only the light from the central galaxy regions. With increasing redshift, the fraction of the galaxy light integrated by the fibers also increases. Comparing measurements obtained from different integration fractions of the galaxy introduces a bias in the results, and aperture effects must be accounted for. IFS enables extracting spectra by integrating the datacubes in different apertures to study how the galactic parameters change with the aperture. In this way, we are able to simulate observations obtained with different fixed-size fibers or, which would be equivalent, observations with a fixed-size fiber of galaxies at different redshifts. This has been studied in detail in Iglesias-Páramo et al. (2013) with Hα emission, in Iglesias-Páramo et al. (2016) for oxygen abundances using the whole CALIFA galaxy sample, and in Gomes et al. (2016) with CALIFA early-type galaxies.

We calculated the spectra within 12 circular apertures centered on the galaxy cores and increasing the radii from 3 to 36″ in steps of 3″. The same procedure as was used for the individual spaxels was applied to measure the metallicities from each of the increasing aperture spectra. The left panel of Fig. 7 shows the average values of the oxygen abundance for each SN type host as a function of an increasing aperture. The measurements within the AGN region of the BPT diagram were not considered when we constructed the averages of this measurement. In the right panel we show the same measurements, but changed the radial scale to the disk effective radius of each galaxy. The differences between the central and the total values shown in the previous subsection arise here with the intermediate behaviors. The average gas abundances decrease with increasing the aperture, and the hosts of the three SN types remain ordered as is shown in the total distributions (see Fig. 2). The SN Ia band lies above the two CC SN bands, and SN II show lower values than SN Ibc host galaxies. This behavior is easily explained (and expected) by the presence of metallicity gradients. As the aperture increases, new regions that are farther from the center are included in the integrated spectra. If these new regions are metal-poorer than their inner counterparts, the average of the aperture would be reduced, but not at the level of the metallicity of the new regions. It is likewise remarkable that in the two figures the SN Ia galaxy band is shallower than the CC SN host bands. Although passive galaxies are not included in the SN Ia group, we show in Appendix B that the metallicity gradients of SN Ia hosts were also shallower. The largest difference for any SN host is around 0.04 dex, and this would be an estimation of the systematic error when using fiber spectra measurements of galaxies spanning a wide range of redshifts.

A similar approach was used by González Delgado et al. (2015), who instead of studying how the stellar metallicity varies at increasing circular apertures studied the deprojected radial profiles and gradients, splitting 300 galaxies of the CALIFA sample according to morphology and mass. Their results agree with our findings. Elliptical and S0 galaxies have higher stellar metallicities and flatter gradients than the late-type galaxies. This corresponds to our SN Ia group since these types of galaxies only host thermonuclear supernovae.

5. Discussion

5.1. Total metallicity

We have shown that the gas-phase and the mass-weighted stellar metallicities derived from the integrated galaxy spectra behave differently for the three SN types (Fig. 2). The average gas-phase metallicity for the three SN types is nearly equal, with differences smaller than 0.01 dex. The distributions are also similar. However, both CC SN types, Ibc and II show a more extended tail toward low metallicity; this tail is more prominent for SNe II. The average mass-weighted stellar metallicity, on the other hand, shows differences of ~0.05 dex between the three SN types. This

[3] The width of the distribution for SNe Ia larger, but this is because of a single deviating point. When this point is removed, the distribution becomes the narrowest of all with a standard deviation 0.03 dex.

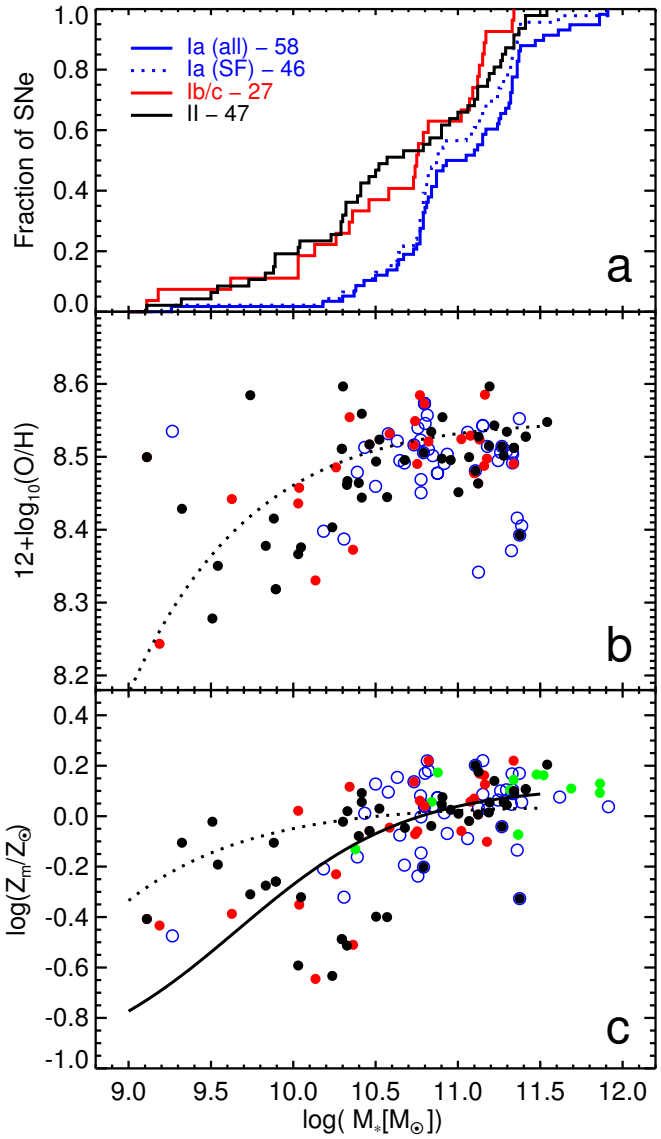

Fig. 8. **a)** Cumulative distributions of the galaxies stellar mass; **b)** mass vs. gas-phase metallicity. The dotted line is the $M-Z$ relation from Sánchez et al. (2013) converted from PP04 to the M13 version of the O3N2 calibrator. **c)** mass vs. mass-weighted stellar metallicity. The dotted line is the $M-Z$ relation from Sánchez et al. (2013) and the solid line is the Panter et al. (2008) relation. The green dots show the elliptical SN Ia hosts.

behavior results from the mass distribution of the galaxies in our sample on one hand and the shape of the mass-metallicity ($M-Z$) relation for the gas-phase and the stellar metallicities on the other.

Figure 8a shows the cumulative distribution of the current stellar mass of the galaxies in our sample by SN type. As already noted in Paper I, the mass distribution shows 0.3–0.4 dex difference between the mean masses of SN Ia hosts and those of the two CC SNe types. Moreover, about 90% of the SN Ia hosts and 60–70% of the CC SN hosts have masses higher than $\log(M/M_{\odot}) \simeq 10.3$ dex.

The $M-Z$ relations for the gas-phase metallicity and mass-weighted stellar metallicities are shown in Fig. 8b and c. The dotted lines in Figs. 8b and c show the $M-Z$ relation for the gas-phase metallicity derived by Sánchez et al. (2013) from CALIFA observations. This relation describes the $M-Z$ relation for

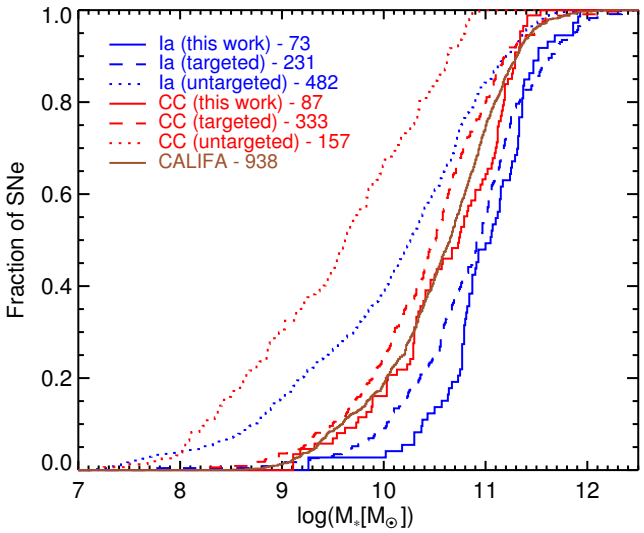

Fig. 9. CDFs of the host galaxy masses of various SN Ia and CC SNe samples (see the text for details).

the gas-phase metallicity of the galaxies in our sample very well[4], but Fig. 8c shows that the mass-weighted stellar metallicity $M-Z$ relation is much steeper, in accordance with the findings of González Delgado et al. (2014). The solid line in Fig. 8c shows the Panter et al. (2008) $M-Z$ relation, which clearly describes the stellar metallicity $M-Z$ relation better. Both the gas-phase and the stellar metallicity $M-Z$ relations clearly present lower scatter above $\log(M/M_{\odot}) \simeq 10.4$ dex.

The gas-phase $M-Z$ relation is tighter and flatter than the stellar metallicity and $\gtrsim$80% galaxies in our sample have masses higher than $\log(M/M_{\odot}) \simeq 10.3$ dex. This is the main reason for the very small differences between the average gas-phase metallicities for the three SN types. On the other hand, the stellar metallicity $M-Z$ relation is steeper, and this is the most likely reason for the observed larger differences in the average stellar metallicities.

The small differences between the total gas-phase metallicity of different SN type host galaxies that we find is somehow at odds with the previously reported larger differences (see, e.g., Prieto et al. 2008; Shao et al. 2014). This is most likely due to the bias toward higher masses in our sample, however. To clarify the possible effect on our results of this bias, we extended the study with data from the literature. Figure 9 shows the CDFs of the host masses of our SN Ia and CC SN samples, including the galaxies with SNe outside of FoV, compared to the targeted and the untargeted samples from Neill et al. (2009), Kelly et al. (2010), Kelly & Kirshner (2012), Childress et al. (2013), Stoll et al. (2013), and Pan et al. (2014). Table 6 gives details of the properties of the corresponding distributions. In these works different IFMs have been employed, and we applied small corrections (~0.04–0.20 dex; Bell et al. 2003; Sullivan et al. 2010) to convert the masses into a Salpeter (1955) IMF. However, additional systematic differences are almost certainly present because different recipes were used to construct the fitting galaxy templates, different observational data were used (photometry and spectroscopy), and different

[4] Strictly speaking, this relation is derived for oxygen abundance at the effective radius r_e. However, as Sánchez et al. (2013) also noted, we found that the difference between the metallicity at r_e is very close to the total metallicity estimated from the integrated spectra. The average difference we found was ~0.02 dex with 1σ scatter around 0.03 dex.

Table 6. Statistics of the galaxy mass distributions in different SN samples in units of $\log(M/M_{\odot})$.

	SN Ia			CC SN		
	mean	σ	median	mean	RMS	median
This work	11.00	0.50	11.06	10.61	0.62	10.74
Targeted	10.85	0.66	10.94	10.42	0.68	10.51
Untargeted	10.08	0.98	10.27	9.52	0.88	9.62

Notes. For each SN subtype we show the mean, the standard deviation σ, and the median.

fitting approaches. Quantifying these differences is beyond the scope of this paper, but they should be kept in mind when combining galaxy masses from different sources.

The data from the literature clearly show that the targeted surveys suffer from a bias toward massive galaxies, which is ∼0.77 dex for SNe Ia and ∼0.9 dex for the CC SNe. It is also evident that our sample, which consists of SNe discovered by targeted searches, is biased even more toward higher masses; with respect to the targeted sample from the literature, this bias for both SN Ia and CC SN is ∼0.15 dex. The mean masses of both SN Ia and CC SNe hosts found in targeted searches are in the range $\log(M/M_{\odot}) \simeq 10.4-10.7$ and with only a small fraction of SNe (∼10 and 20 % for SN Ia and CC SN, respectively) present in galaxies with masses below $\log(M/M_{\odot}) \simeq 10.3$ dex. Because of the lower scatter in the $M - Z$ relation above $\log(M/M_{\odot}) \simeq 10.3$ dex, the metallicity differences between the SN types are probably small in samples from targeted searches. The untargeted searches, on the other hand, include galaxies with lower masses in the range where the $M - Z$ relation is steeper and the metallicity differences, if significant, will be more pronounced.

5.2. Local metallicity

We have estimated both the gas-phase and stellar metallicities at the SN locations. As discussed in Stanishev et al. (2012), the stellar metallicities are estimated with much greater uncertainty because of the various factors that were used, including astrophysical and numerical degeneracies, noise in the observed spectra, uncertainties in the recipes to construct the SSPs, etc. Even without these uncertainties, the S/N in the continuum of the binned spectra at the SN location may not be enough to estimate the metallicity accurately enough. For this reason we focus our discussion on the local metallicity to the gas-phase oxygen abundance.

We found only small differences between the average metallicity at the SN locations for the three SN types, 8.522, 8.500, and 8.484 dex for SN Ia, Ibc, and II, respectively. These differences are considerably smaller than the 1σ scatter, which is 0.056 dex for SN Ia and 0.112 dex for the CC SNe. However, we need to clarify whether we measureed the local metallicity at the SN position. With increasing distance to the galaxies, it becomes more difficult to measure local quantities because the spatial resolution decreases when we observe with fixed-size slits or fibers. Recently, Niino et al. (2015) studied how the variation of the metallicity within a galaxy and the spatial resolution affect the local metallicity estimation. They found that when the resolution is lower than 500 pc, the local metallicity could be accurately estimated. A resolution of up to 1 kpc also provides reasonable estimates, although some systematic effects are present. When the resolution is higher than 1 kpc, the constraint of the local metallicity becomes more uncertain. For the redshift range of our targets from 0.005 to 0.03, the resolution of the CALIFA maps (PSF ∼ 2.57 arcsec) corresponds to a spatial resolution between ∼250 pc and 1.5 kpc. However, only a small fraction of our targets are at the higher end of the redshift distribution, and on average, the resolution effects will be small in our sample.

It is expected that the differences between the local metallicities of the different SN types in our sample are small are because the total metallicities estimated from the integrated spectra are on average also the same and the galaxies seem to have a characteristic metallicity gradient in normalized radii units. This means that large differences between the local metallicities can be observed if (i) the different SN types have significantly different radial distributions or (ii) the galaxies contain regions with metallicities that are significantly different from the galaxy average. In the latter case, if certain SN type prefers to explode in a low- or high-metallicity environment, then the local metallicity of this SN type will tend to differ from the galaxy average. However, a careful inspection of the 2D metallicity maps shows that regions with a metallicity that significantly differs from average are rare or absent because the dynamical range of abundances across the entire galaxy is small.

The analysis of the SN radial distances shows that SNe Ibc tend to explode slightly closer (by less than 1 kpc) to the galaxy center than SNe II, and SNe Ia on average 1 kpc farther away than SNe II. However, when the distances are normalized to the effective radius $R_{\rm eff}$, all distributions have similar averages of 1.1, 1.0, and 1.2 $R_{\rm eff}$ for SN Ia, Ibc, and II, respectively. This agrees with previous statistical studies of SNe radial distributions (Bartunov et al. 1992; van den Bergh 1997; Tsvetkov et al. 2004; Petrosian et al. 2005; Prieto et al. 2008; Hakobyan et al. 2009; Anderson & James 2009). The upper panel of Fig. 10 shows the distribution of the deprojected distances measured in disk effective radius units. In the bottom panel of Fig. 10 the difference between the local and the total metallicities as function the normalized deprojected distances is shown. The difference decreases with the radial distance for all SN types at a rate consistent with the average metallicity gradient (the line with a slope of −0.074 guides the eye). The figure shows that SNe Ia tend to be slightly above the line and hence they show a larger average difference than the CC SNe. However, the difference is rather small and could be caused by other effects, for example, by a slightly biased estimation of the total galaxy metallicity.

Figure 10b shows that the metallicity at the SN location follows the galaxy mean metallicity and that it also changes with the radial distance following the metallicity gradients. However, the scatter of the difference between the local and the total metallicities, and the scatter around the line is considerable, ∼0.05 dex. One interesting question is whether part of this scatter arises because some SNe preferably explode in regions with higher metallicities. Many galaxies have negative metallicity gradients, which means that if this were the case, SNe may tend to explode closer to the galaxy center. However, the density of the stars in the galaxies and the SFR also increase toward the center, and it is statistically expected to find more SNe toward the central regions. Thus, the two effects will be difficult to distinguish.

Galaxies typically have central symmetry. One way to test the hypothesis that some SNe prefer to explode in high-metallicity regions is to consider the difference between the metallicity at the SN position and the mean value of the galaxy metallicity at the radial distance of the SN. To estimate the latter, we computed the mean metallicity and the standard deviation of the individual spaxels within 1 kpc of the deprojected GCD of the SNe. Figure 11 shows the distributions of the differences

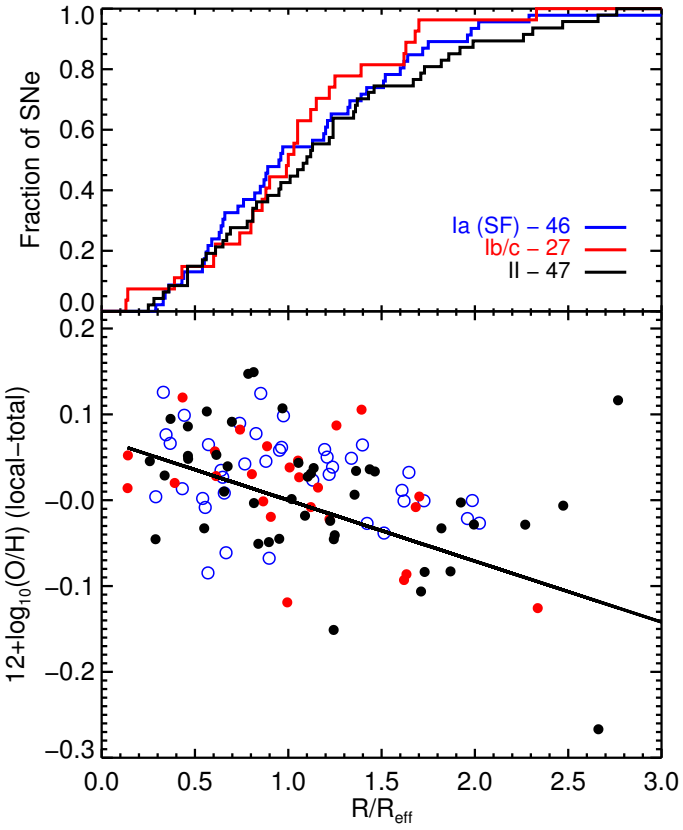

Fig. 10. *Upper panel*: CDFs of the normalized radial distribution of the different SN types. *Lower panel*: difference between the local and the total metallicity as a function of the normalized GCD. The line is a guide to the eye and has a slope of −0.074, which is the average metallicity gradient of the galaxies in our sample.

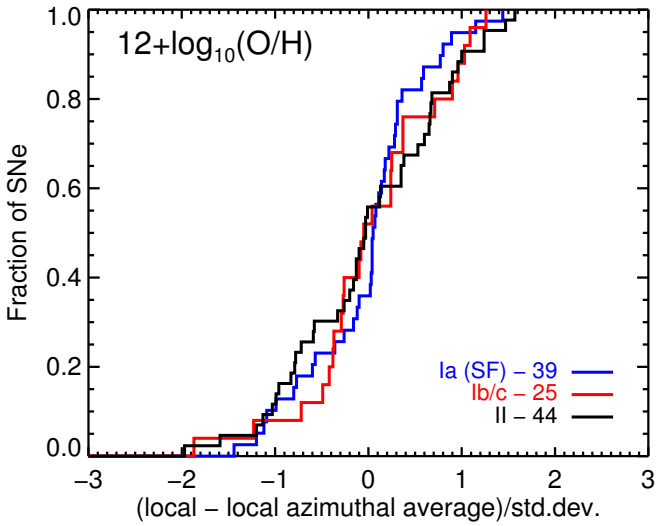

Fig. 11. Difference between the oxygen abundance at SN position compared to the azimuthal average at that distance, normalized to the standard deviation of the abundance at that distance.

divided by the standard deviation. For all SN types the mean differences are essentially zero, and the distributions are narrow with standard deviations of about one. SN II show a slightly wider distribution than the other SN types. This indicates that on average the metallicity at the SN location does not differ significantly from the galaxy average at the SN radial distance. There is only a small hint for an extended tail toward lower metallicities for SN II.

5.2.1. Proxies of local metallicity

We have compared the directly estimated local metallicites obtained with IFS with several other approaches that have been used as proxies of local metallicity estimations. We conclude that the central metallicity, with and without a correction assuming that the characteristic metallicity gradient, is the least accurate. It has both a larger bias and a larger scatter. As expected, the metallicity of the closest H II region and the metallictiy estimated from each galaxy's individual metallicity gradient are the best proxies of the local metallicity. However, these two methods are applicable to nearby galaxies alone and are most likely of little practical use, for instance, for high-redshift SN Ia studies. On the other hand, the total galaxy metallicity appears to be the best compromise. It has a relatively small bias and scatter. In addition, this quantity can be easily measured for galaxies at high redshifts.

The probable reason for the similarity between the local and total metallicities is that the metallicity gradients in low-redshift galaxies are fairly shallow. However, we recall that this may not be the case for high-redshift galaxies, and therefore the total metallicity may not be as good a proxy as at low redshift.

5.2.2. Differences among SN subtypes

Our primary goal is to explore the connection between the SN environmental metallicity and the nature of the progenitors for each SN type. At present, the CALIFA sample we used in our analysis is not sufficiently large to allow splitting the two main CC SN groups into more subclasses with enough events. In addition, the vast majority of our sample comes from targeted searches and is biased toward high-mass, metal-rich galaxies. As a result, the local metallicity we measure is very similar for all SNe. For these reasons we combined our values with measurements of the metallicity at SN locations from the literature. This enlarged sample contains SNe discovered by both targeted and untargeted surveys. We considered only measurements performed at the SN location or in the close vicinity, and whenever repeated, we relied on our measurements. The compiled sample includes all the measurements from Thöne et al. (2009), Young et al. (2010), Modjaz et al. (2011), Anderson et al. (2011), Prieto et al. (2012), Kuncarayakti et al. (2013a,b), Tomasella et al. (2013); and only those reported as local from Anderson et al. (2010), Leloudas et al. (2011), Sanders et al. (2012), Habergham et al. (2012), and Moreno-Raya et al. (2016). In addition, we included metallicities of 11 SNe in galaxies observed with the new MUSE IFS (Galbany et al. 2016a). Following Sanders et al. (2012), we did not include results of Kelly & Kirshner (2012) since those are measurements from the center of the galaxies.

Since many different calibrators were used, we considered only those obtained using the PP04 O3N2 calibrator and converted them into the M13 scale. However, this sample can be further enlarged if we also consider those measurements computed with the PP04 N2 calibrator, and converted into O3N2 scale using the relation produced by Kewley & Ellison (2008). In this enlarged sample we used data from Stoll et al. (2013), Sahu et al. (2009), Levesque et al. (2010), Milisavljevic et al. (2013), Inserra et al. (2013), Van Dyk et al. (2012), Taddia et al. (2013, 2015). We also added the metallicities of the SN Ia hosts

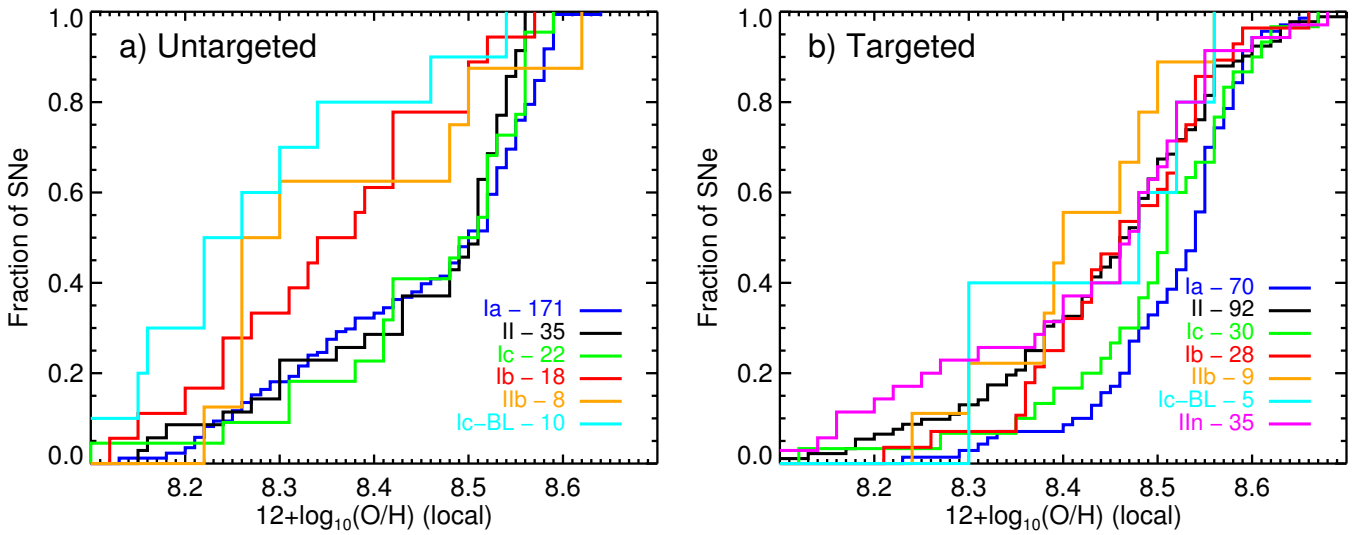

Fig. 12. Compilation of the oxygen abundances at the SN location measured in this work combined with previously published results from the literature. We combined published measurements using the O3N2 calibrator with measurements using the N2 converted to O3N2 with Kewley & Ellison (2008) relation. **a)** for SNe discovered in untargeted searches; **b)** in targeted searches. The CALIFA sample presented in this work contributes essentially to the targeted sample.

Table 7. Statistics of the local metallicity distributions of SNe discovered in untargeted and targeted searches.

	Untargeted					Targeted				
Type	Mean	σ	σ_m	Median	N_{SN}	Mean	σ	σ_m	Median	N_{SN}
Ia[a]	8.455	0.129	0.010	8.503	171	8.520	0.083	0.010	8.543	70
Ic	8.458	0.124	0.026	8.515	22	8.495	0.112	0.020	8.511	30
II	8.447	0.126	0.021	8.511	35	8.450	0.127	0.013	8.475	92
IIb	8.367	0.149	0.053	8.302	8	8.415	0.101	0.034	8.404	9
Ib	8.355	0.130	0.031	8.388	18	8.461	0.102	0.019	8.468	28
Ic-bl	8.274	0.151	0.048	8.261	10	8.436	0.123	0.055	8.481	5
Ib/IIb	8.359	0.133	0.026	8.344	26	8.450	0.100	0.016	8.448	39
Ibc	8.418	0.133	0.020	8.428	44	8.485	0.107	0.014	8.511	62
IIn			–			8.427	0.150	0.025	8.475	35
CC	8.421	0.137	0.015	8.488	88	8.455	0.126	0.009	8.481	196

Notes. For each SN subtype are shown the mean, the standard deviation σ, the standard deviation of the mean σ_m, the median, and the number of SNe. [(a)] The metallicities of the untargeted SN Ia sample come from Pan et al. (2014) and Childress et al. (2013). These measurements correspond to the total galaxy metallicity and have been corrected by +0.028 dex to account for the bias. See text for details.

from the untargeted searches reported in Pan et al. (2014) and Childress et al. (2013). These metallicities were measured with long-slit spectroscopy, and the manner in which the spectra were extracted from the 2D images means that they are close to the galaxy total metallicity. However, in our sample the local and the total metallicities of SN Ia hosts differ on average by 0.029 dex, and we can use the Pan et al. (2014) and Childress et al. (2013) measurements as proxy of the local metallicity.

We considered the following main SN classes: Ia, Ib, Ic, broad-line Ic (IcBL), II, IIn, and IIb. I has recently been questioned whether there truly are two different populations of SN II (IIP and IIL). While some works (Arcavi et al. 2012; Faran et al. 2014) presented evidence for two separated populations, this has been questioned by a number of works (Anderson et al. 2014; Sanders et al. 2015; Galbany et al. 2016b), which argued that this is really a continuous between slow- and fast-decliners, and the traditional division was due to the low number of SNe IIL. Following the latter works, we assigned SNe IIP and IIL to one group II. We also considered separate classes of SNe Ib and IIb, but because they are probably closely related (by a continuous sequence of the amount of hydrogen in their outer layers), we also computed the mean metallicity of SNe Ib and IIb together. Many SNe Ib/c have an uncertain classification. They were grouped with SNe Ib/c with a certain classification to compute the mean metallicity of the combined SN Ib/c class. The mean metallicity of the whole CC SN class was also computed excluding the broad-line SNe Ic.

Furthermore, the sample was divided into two groups: SNe discovered by targeted or untargeted searches. The resulting distributions of the oxygen abundance are shown in Fig. 12. The properties of the distributions for all SN types are summarized in Table 7, and the p-values of the KS tests are listed in Table 8. The CALIFA sample presented in this work comprises mostly SNe discovered in targeted searches and therefore only significantly contributes to the targeted SN sample.

Metallicity at the SN Ia locations

The locations of SNe Ia are most likely not related at all to the birth place of the progenitor star because of their long delay

Table 8. *P*-values of the KS test for the local distributions presented in Fig. 12.

	Targeted	Untargeted
Ia–II	0.0002	0.0975
Ia–Ic	0.1434	0.6226
Ia–Ib	0.0108	0.0037
Ia–Ibc	0.0633	0.0420
Ia–IIb	0.0075	0.0690
Ia–Ic-BL	0.4416	0.0029
Ia–Ib/IIb	0.0004	0.0008
Ia–CC	0.0001	0.0202
II–Ic	0.0944	0.6855
II–Ib	0.7992	0.0038
II–Ibc	0.0886	0.1209
II–IIb	0.6427	0.0964
II–Ic-BL	0.8178	0.0068
II–Ib/IIb	0.7849	0.0034
Ic–Ib	0.3380	0.0622
Ic–IIb	0.0568	0.0439
Ic–Ic-BL	0.6309	0.0054
Ic–Ib/IIb	0.0537	0.0400
Ib–IIb	0.5754	0.6524
Ib–Ic-BL	0.6546	0.2813
IIb–Ic-BL	0.6342	0.1912

times (100 Myr to Gyr), therefore progenitors might have traveled a considerable distance across the galaxy before exploding as supernovae. Any association between the observed properties of the SN environment and the SN progenitor population is much more problematic. The study of the properties of SN Ia environments can give insights on the characteristics of the explosion, however, which might be useful for cosmological analyses, for example.

SNe Ia have the highest mean metallicity at the SN location in the targeted sample (8.52 dex), and the mean metallicity is similar to SN II and Ic in the untargeted (8.46 dex). However, most of the untargeted SN Ia come from measurements similar to the total metallicity, corrected for the small bias. The sample of Pan et al. (2014) has a higher mean metallicity 8.53 dex (corrected for the bias), but the mean of the whole sample is pushed toward low metallicity by the sample of Childress et al. (2013). The reason is that the latter sample also has a significantly lower mean mass.

When the mean masses of SN Ia hosts from Table 6 in the targeted and untargeted samples are taken together and the corresponding metallicities are computed with the $M - Z$ relation of Sánchez et al. (2013), we obtain 8.53 and 8.47 dex for SNe Ia in the combined targeted and untargeted samples, respectively. The same analysis for CC SNe hosts gives metallicities of 8.50 and 8.36 dex. However, when we apply the $M - Z$ relation to our sample alone, we obtain metallicities of 8.53 and 8.50 dex for SN Ia and CC SN hosts, respectively. These numbers are very close to the actual estimated mean metallicities, except for CC SNe in the untargeted sample, which deviate by 0.06 dex. This suggests that the difference in the mean metallicity of the different samples is to a large extent due to the $M - Z$ relation.

Metallicity at the CC SN locations

Table 7 shows that all SN types, except for SN II, show a bias toward higher metallicity in the targeted samples. The bias is different for the different types, and SN Ib and Ic-BL are particularly affected (>0.1 dex). In the targeted sample SN Ic locations show higher Z than both SN Ib and SN II locations, and the latter also show Z similar to SN IIn and SN Ic-bl. SN IIb is the CC SN subtype with the lowest average Z. This changes for the untargeted sample: while SN II and SN Ic now show similar Z, SN Ib have significantly lower Z, but are, similar to SN IIb. SN Ic-BL, in the lowest Z end, as expected. Based on the untargeted SNe, we therefore obtain the following sequence:

$$Z_{\rm Ic} \gtrsim Z_{\rm II} > Z_{\rm Ib} \gtrsim Z_{\rm IIb} > Z_{\rm Ic-BL}. \quad (1)$$

The differences in the mean local metallicites are generally small and insignificant in most cases. The KS test indicated that SNe Ic and II probably came from the same metallicity distribution, which is different from that of SN Ib, IIb, and Ic-BL.

Furthermore, we studied how the number ratios between two subtypes evolve with the environmental metallicity increase. Figure 13 presents the results of several of these ratios measured in three metallicity bins centered on 8.16 (below solar), 8.38 (around solar), and 8.60 dex (above solar). The analysis is split for untargeted and targeted samples.

In general, the behavior of the ratios is different in the targeted and untargeted samples, with the exception of the Ib/Ic ratio, which decreases with metallicity in both samples. While in the untargeted sample the Ic/II ratio is practically flat with a soft increase to high metallicity, in the targeted sample it clearly increases. As Fig. 12 showed, there is no significant difference in the untargeted SN Ic and II distributions, while the difference is higher in the targeted sample. We also found an increasing rate of targeted SNe Ibc over SNe II, as previously found by Arcavi et al. (2010), Prantzos & Boissier (2003), Prieto et al. (2008) and Kelly & Kirshner (2012). However, when we consider only the untargeted sample, this ratio develops in the opposite direction. By studying the relative rates between the different components, we see that this evolution is driven by the decreasing number of SNe Ib at higher metallicities: while the ratio between Ib and II is practically flat for the three regimes in the targeted sample, it steeply decreases in the untargeted sample. Therefore, any difference in the evolution of SN Ibc when compared to SN II is caused by the lower metallicity of SN Ib compared to Ic in targeted or untargeted samples.

In addition, the proportion of SNe Ia in all CC SN types increases with the environmental metallicity, as we found in this and previous sections: although SNe Ia also occur in metal-poor environments, their ratio is significantly higher in the metal-rich regime than in all CC SN types. The increase is more pronounced in the targeted sample and flatter in the untargeted sample.

Influence of metallicity on determining the CC SN subtype

Differences in the evolution of SN type ratios with metallicity may be used to connect SN types to possible progenitor scenarios. Both the wind strength and the binary mass transfer rate are plausible scenarios through which SNe Ibc lose their external layers. Another possibility may be that external H and He layers of the progenitor suffer severe depletion by enhanced mixing that prevents us from detecting them (Frey et al. 2013), although this would be difficult to assess based on environmental studies.

According to the models based on the evolution of single massive stars (e.g., Heger et al. 2003; Georgy et al. 2009), both high metallicities and high initial masses are required to produce SNe Ibc in single stars, while in binary systems the mass loss is dominated by mass transfer and the models predict a less significant trend with metallicity. If the primary SN Ibc progenitor

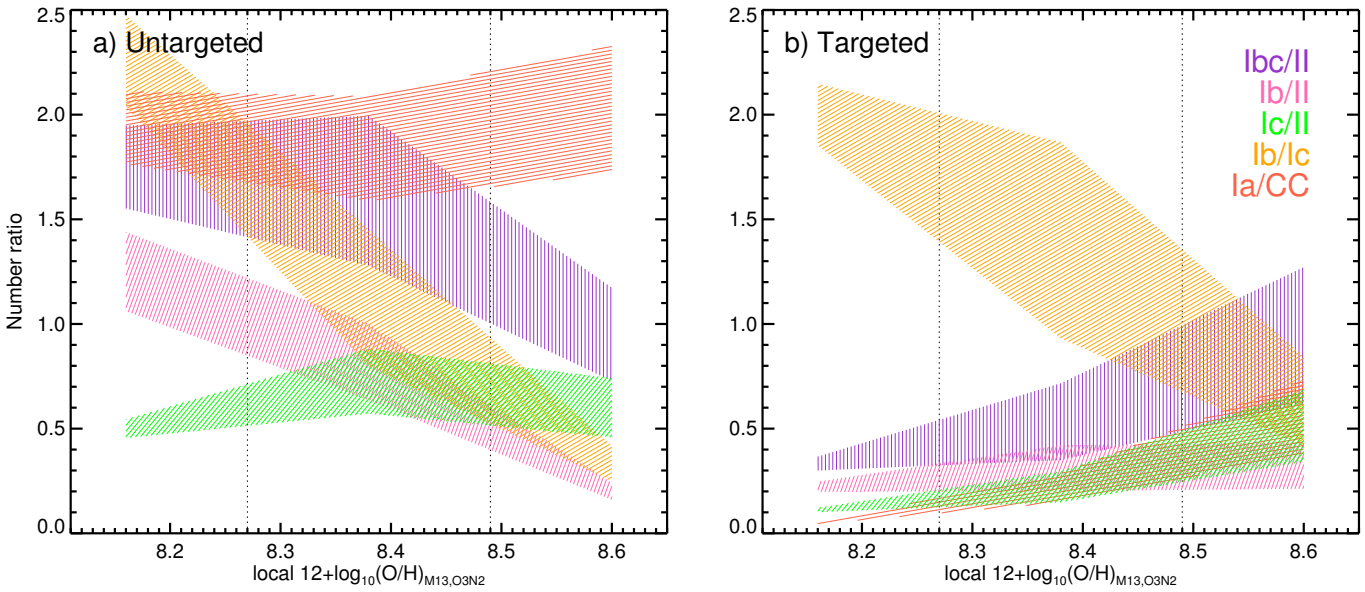

Fig. 13. Ratio of SN subtypes as a function of local metallicity from the compilation of the oxygen abundances at the SN location measured in this work combined with previously published results from the literature. **a)** for SNe discovered in untargeted searches; **b)** in targeted searches.

channel is a single WR star, then the rate of SN Ibc relative to SNe II would be enhanced at higher metallicities. Although this is what we found when considering SN discovered in targeted searches, this becomes more complicated in untargeted SN: while the ratio between SN Ibc and II decreases with increasing metallicity, it is driven by the lower local metallicities at SN Ib positions. The strongest result we found is that SNe Ic, which are stripped of their H and He external layers, occur on average in significantly higher metallicity environments than SN Ib, which only lack the H envelope. These SN progenitors are in general short-lived, which means that the SN local environmental metallicity is more likely related to the metallicity of the progenitor. The ratios presented in Fig. 13 imply that at least a part of the progenitors of SNe Ic are single stars in strong metallicity-driven wind environments, while the remaining SN Ic and a significant part of SN Ib and also SN IIb arise from binary progenitors (Claeys et al. 2011; Sana et al. 2012). This is supported by the results from Kuncarayakti et al. (2013a), who inferred lower masses from the stellar population ages for SN Ib than for SN Ic. In addition, the flat ratio of untargeted SN Ic over SN II would imply that metallicity does not play a role between these types, and that other factors (e.g., progenitor mass) might be more important.

On the other hand, the radial distributions of different SNe types (see Sect. 5.2) have been used as a proxy of environmental metallicity. If the central regions of galaxies have a higher metallicity, we can argue based on distance distributions that the progenitors of SNe Ibc, which are more centered, should be metal-richer than those producing other SNe types. This argument is consistent with the models claiming that SNe Ibc progenitors are massive stars whose envelopes have been stripped by stellar winds that were driven by metallicity before explosion (Puls et al. 1996; Kudritzki & Puls 2000; Mokiem et al. 2007). Since stars in higher metallicity environments suffer from stronger driven winds, SNe Ibc progenitors lose more mass through these winds before explosion than SNe II, which are on average located farther away and reside in lower metallicity environments. However, we showed in Sect. 3.2 that a significant fraction of SN host galaxies (~30%) present a decreasing gradient toward the center, which, when it is accounted for, would imply lower environmental metallicities for objects closer to the center in those galaxies.

These two findings together question the importance of metallicity as the relevant factor in determining the SN type and supports that at least a fraction of the SNe might come from binary systems. The findings are compatible with a location of the SNe at lower radial distances. This also agrees with results of Habergham et al. (2012) and Anderson et al. (2015), who found that SN Ibc are more centralized than SNe II in interacting galaxies, where metallicity gradients are flatter or absent, indicating that other effects play a role in determining the SN type in addition to metallicity.

6. Conclusions

We present an updated sample of 115 galaxies with mean redshift $z = 0.015$ observed with IFS by the CALIFA survey. These galaxies host 132 SNe (47 type II, 27 type Ib/c+IIb, and 58 Ia) that were within the FoV covered by the instrument. The spatially resolved spectroscopy used in this work has several advantages with respect to most commonly used approaches, namely multi-wavelength photometry and fiber or slit spectroscopy. IFS allows obtaining 2D maps of the most important parameters from both the stellar populations and the ionized gas emission. Following our previous work on the role of the local star-formation in determining the SN type, presented in Paper I, here we focused on studying and comparing the environmental metallicity for the various SN types. The relevance of this study arises from the influence of the SN progenitors metallicity on the supernova explosion and possible implications in high-redshift supernova studies and determination of cosmological parameters with SN. Our main goals were to 1) unveil possible relations between the host metallicity at the SN location and the properties of the supernova or their progenitors; 2) identify systematic errors of the various proxies commonly used to infer the host metallicity at SN locations or the metallicity of the SN progenitors; and 3) estimate the accuracy in the determination of the local metallicity of the various proxies in high-redshift supernova

studies. To achieve a better comparison between galaxies, the radial dependence of galaxy properties was studied in units of the galaxy disk effective radius. We determined the galaxy disk effective radius by fitting a pure exponential function to their brightness profile and calculated the metallicity gradients for all galaxies. Different proxies for estimating the local metallicity were used, which allowed us to search for differences among SN types. It also allowed us to compare different proxies and study their accuracy. Our main findings are summarized below.

- The gas-phase average metallicity at SN location shows significant differences of ∼0.04 dex between SN Ia and SN II, while the mass-weighted stellar metallicity at the SN location shows no significant difference between the three main SN groups.
- The total gas-phase metallicity distributions are indistinguishable among the SN groups (centered around 8.49 dex), while the total stellar metallicity distribution for SNe Ia is slightly shifted to higher values than SN II ($\langle Z_{\rm Ia}\rangle - \langle Z_{\rm II}\rangle$ = 0.015).
- The difference between the local and the total metallicities are on average small as well, and are only significant for SN Ia (0.03 dex). The reason is probably that the sample is biased toward galaxies with high masses; most galaxies have $\log(M/M_{\odot}) > 10.3$ dex.
- Several proxies of the local metallicity were studied. The most accurate proxies are those using the galaxy metallicity gradient plus the SN galactocentric distance and the metallicity of the closest HII region from the SN.
- The total galaxy metallicity is also a good proxy of the local metallicity for CC SNe, although we find a significant shift of ∼0.03 dex for SNe Ia. We also find that weak AGNs that cannot be seen in the total spectrum may only weakly bias the metallicity estimate from the galaxy-integrated spectrum by 0.03–0.04 dex. These results are encouraging for high-redshift studies because it allows the local metallicity to be estimated, although the possible evolution of the metallicity gradient in galaxies with redshift may render this proxy less accurate.
- On the other hand, we find that the central metallicity, with and without correction for the characteristic metallicity gradient, is the least accurate proxy. It shows significant differences for both gas-phase and stellar metallicity. The reason might be that about 30% of the galaxies show a metallicity decrease toward the center; another 10% show only a flattening.
- The local metallicity at the SN positions is not significantly different from the mean galaxy metallicity at the galactocentric distance of the SN. This argues against the hypothesis that certain SN type may prefer to explode in environments with a specific metallicity.
- When the galaxy masses of our sample were combined with those from the literature, it became clear that the targeted SN searches were biased toward high-mass galaxies. The average bias is $\log(M/M_{\odot}) = 0.8$.
- By extending our SN sample with published measurements of the metallicity at the vicinity of the SN, we studied the metallicity distributions for all SN subtypes split into SN discovered in targeted and untargeted searches. We confirm the known fact that the targeted searches are biased toward high metallicity.
- For the SN discovered in targeted searches, for which our sample is representative, we find that SN Ia and Ic have the highest metallicity of all other SN types. The differences are small, however, and in most cases are statistically insignificant.
- In the untargeted searches, SN Ia, Ic, and II have a higher metallicity than the other SN types. It therefore appears that the local metallicities of SN Ib and IIb that are significantly different from those of SN Ic.
- By studying the evolution of the ratios between pairs of subtypes as a function of the metallicity, we found that the ratio of SN Ibc and II decreases with metallicity. This is driven by the significantly lower metallicity of SN Ib. This supports the hypothesis that SN Ib result from binary progenitors and (at least some) SN Ic result from single stars that are stripped of their outer H and He layers by strong metallicity-driven winds.

The CALIFA survey has proven that integral field spectroscopy is a powerful tool for SN environmental studies, in addition to the main aims of the survey, which were the study of galaxy formation and evolution. The Sydney-AAO Multi-object Integral-field spectrograph (SAMI Croom et al. 2012) and Mapping Nearby Galaxies at APO (MaNGA, (Bundy et al. 2015)) are currently the largest IFS surveys and will increase the statistics by a factor ∼5 to 20. However, they both lack high spatial resolution, which is needed to avoid the systematics effects studied in this work. Kuncarayakti et al. (2013a,b, 2015) performed a similar study as the one presented here and in Paper I, but they studied the SN parent stellar clusters with resolutions of ∼60 pc. Although this high resolution allows properly distinguishing among stellar clusters, the small field of view does not allow comparisons between local and other estimates of galaxy parameters across the galaxy. The advent of the new generation of instruments, such as the Multi-Unit Spectroscopic Explorer (MUSE) Integral Field Unit recently mounted on the 8m VLT UT4 (Bacon et al. 2010), will provide the required high spatial resolution together with a larger field of view. This combines the two requirements (see Sánchez et al. 2015; Galbany et al. 2016a; Anderson et al. 2015). This and other CALIFA studies will be improved with such a combination of these two factors.

Acknowledgements. We acknowledge Joseph P. Anderson and Hanindyo Kuncarayakti for fruitful discussions on SN environments (among many other topics). This work was partly funded by FCT with the research grant PTDC/CTE-AST/112582/2009. Support for L.G. is partially provided by FCT, by CONICYT through FONDECYT grant 3140566, and from the Ministry of Economy, Development, and Tourism's Millennium Science Initiative through grant IC12009, awarded to The Millennium Institute of Astrophysics (MAS). V.S. acknowledges financial support from Fundação para a Ciência e a Tecnologia (FCT) under program Ciência 2008. C.J.W. acknowledges support through the Marie Curie Career Integration Grant 303912. This study makes use of the data provided by the Calar Alto Legacy Integral Field Area (CALIFA) survey (http://www.caha.es/CALIFA/). CALIFA is the first legacy survey being performed at Calar Alto. The CALIFA collaboration would like to thank the IAA-CSIC and MPIA-MPG as major partners of the observatory, and CAHA itself, for the unique access to telescope time and support in manpower and infrastructures. The CALIFA collaboration thanks also the CAHA staff for the dedication to this project. Based on observations collected at the Centro Astronómico Hispano Alemán (CAHA) at Calar Alto, operated jointly by the Max-Planck Institut für Astronomie and the Instituto de Astrofísica de Andalucía (CSIC). The STARLIGHT project is supported by the Brazilian agencies CNPq, CAPES and FAPESP and by the France-Brazil CAPES/Cofecub program. This research has made use of the Asiago Supernova Catalogue, the SIMBAD database, operated at CDS, Strasbourg, France, the NASA/IPAC Extragalactic Database (NED), which is operated by the Jet Propulsion Laboratory, California Institute of Technology, under contract with the National Aeronautics and Space Administration, IAU Circulars presented by the Central Bureau for Astronomical Telegrams, and data products from SDSS and SDSS-II surveys. We acknowledge the usage of the HyperLeda database (http://leda.univ-lyon1.fr).

References

Aldering, G., Humphreys, R. M., & Richmond, M. 1994, AJ, 107, 662
Alloin, D., Collin-Souffrin, S., Joly, M., & Vigroux, L. 1979, A&A, 78, 200
Anderson, J. P., & James, P. A. 2009, MNRAS, 399, 559
Anderson, J. P., Covarrubias, R. A., James, P. A., Hamuy, M., & Habergham, S. M. 2010, MNRAS, 407, 2660
Anderson, J. P., Habergham, S. M., & James, P. A. 2011, MNRAS, 416, 567
Anderson, J. P., Habergham, S. M., James, P. A., & Hamuy, M. 2012, MNRAS, 424, 1372
Anderson, J. P., González-Gaitán, S., Hamuy, M., et al. 2014, ApJ, 786, 67
Anderson, J. P., James, P. A., Habergham, S. M., Galbany, L., & Kuncarayakti, H. 2015, PASA, 32, 19
Arcavi, I., Gal-Yam, A., Kasliwal, M. M., et al. 2010, ApJ, 721, 777
Arcavi, I., Gal-Yam, A., Cenko, S. B., et al. 2012, ApJ, 756, L30
Arnett, W. D., Bahcall, J. N., Kirshner, R. P., & Woosley, S. E. 1989, ARA&A, 27, 629
Bacon, R., Accardo, M., Adjali, L., et al. 2010, in SPIE Conf. Ser. 7735, 8
Baldwin, J. A., Phillips, M. M., & Terlevich, R. 1981, PASP, 93, 5
Bartunov, O. S., Makarova, I. N., & Tsvetkov, D. I. 1992, A&A, 264, 428
Becker, S. A., & Iben, Jr., I. 1980, ApJ, 237, 111
Bell, E. F., McIntosh, D. H., Katz, N., & Weinberg, M. D. 2003, ApJS, 149, 289
Bersten, M. C., Benvenuto, O. G., Folatelli, G., et al. 2014, AJ, 148, 68
Bethe, H. A., Brown, G. E., Applegate, J., & Lattimer, J. M. 1979, Nucl. Phys. A, 324, 487
Boissier, S., & Prantzos, N. 2009, A&A, 503, 137
Bravo, E., Domínguez, I., Badenes, C., Piersanti, L., & Straniero, O. 2010, ApJ, 711, L66
Bresolin, F., Gieren, W., Kudritzki, R.-P., et al. 2009, ApJ, 700, 309
Bruzual, G. 2007, in From Stars to Galaxies: Building the Pieces to Build Up the Universe, eds. A. Vallenari, R. Tantalo, L. Portinari, & A. Moretti, ASP Conf. Ser., 374, 303
Bundy, K., Bershady, M. A., Law, D. R., et al. 2015, ApJ, 798, 7
Cappellari, M., & Copin, Y. 2003, MNRAS, 342, 345
Childress, M., Aldering, G., Antilogus, P., et al. 2013, ApJ, 770, 107
Cid Fernandes, R., Mateus, A., Sodré, L., Stasińska, G., & Gomes, J. M. 2005, MNRAS, 358, 363
Claeys, J. S. W., de Mink, S. E., Pols, O. R., Eldridge, J. J., & Baes, M. 2011, A&A, 528, A131
Croom, S. M., Lawrence, J. S., Bland-Hawthorn, J., et al. 2012, MNRAS, 421, 872
Crowther, P. A. 2007, ARA&A, 45, 177
de Vaucouleurs, G. 1948, Annales d'Astrophysique, 11, 247
Dessart, L., Hillier, D. J., Livne, E., et al. 2011, MNRAS, 414, 2985
Diaz, A. I. 1989, in Evolutionary Phenomena in Galaxies, eds. J. E. Beckman, & B. E. J. Pagel, 377
Diehl, S., & Statler, T. S. 2006, MNRAS, 368, 497
Dominguez, I., Chieffi, A., Limongi, M., & Straniero, O. 1999, ApJ, 524, 226
Eldridge, J. J., Fraser, M., Maund, J. R., & Smartt, S. J. 2015, MNRAS, 446, 2689
Elias-Rosa, N., Van Dyk, S. D., Li, W., et al. 2011, ApJ, 742, 6
Faran, T., Poznanski, D., Filippenko, A. V., et al. 2014, MNRAS, 445, 554
Fathi, K., Beckman, J. E., Zurita, A., et al. 2007, A&A, 466, 905
Folatelli, G., Bersten, M. C., Benvenuto, O. G., et al. 2014, ApJ, 793, L22
Frey, L. H., Fryer, C. L., & Young, P. A. 2013, ApJ, 773, L7
Fryer, C. L., Mazzali, P. A., Prochaska, J., et al. 2007, PASP, 119, 1211
Gal-Yam, A., & Leonard, D. C. 2009, Nature, 458, 865
Galbany, L., Miquel, R., Östman, L., et al. 2012, ApJ, 755, 125
Galbany, L., Stanishev, V., Mourão, A. M., et al. 2014, A&A, 572, A38 (Paper I)
Galbany, L., Anderson, J. P., Rosales-Ortega, F. F., et al. 2016a, MNRAS, 455, 4087
Galbany, L., Hamuy, M., Phillips, M. M., et al. 2016b, AJ, 151, 33
García-Benito, R., Zibetti, S., Sánchez, S. F., et al. 2015, A&A, 576, A135
Garnett, D. R., Shields, G. A., Skillman, E. D., Sagan, S. P., & Dufour, R. J. 1997, ApJ, 489, 63
Gaskell, C. M., Cappellaro, E., Dinerstein, H. L., et al. 1986, ApJ, 306, L77
Georgy, C., Meynet, G., Walder, R., Folini, D., & Maeder, A. 2009, A&A, 502, 611
Gomes, J. M., Papaderos, P., Vílchez, J. M., et al. 2016, A&A, 586, A22
González Delgado, R. M., Cid Fernandes, R., García-Benito, R., et al. 2014, ApJ, 791, L16
González Delgado, R. M., García-Benito, R., Pérez, E., et al. 2015, A&A, 581, A103
Graham, A. W., Driver, S. P., Petrosian, V., et al. 2005, AJ, 130, 1535
Habergham, S. M., James, P. A., & Anderson, J. P. 2012, MNRAS, 424, 2841
Habergham, S. M., Anderson, J. P., James, P. A., & Lyman, J. D. 2014, MNRAS, 441, 2230
Hakobyan, A. A., Mamon, G. A., Petrosian, A. R., Kunth, D., & Turatto, M. 2009, A&A, 508, 1259
Heger, A., Fryer, C. L., Woosley, S. E., Langer, N., & Hartmann, D. H. 2003, ApJ, 591, 288
Henry, R. B. C., & Worthey, G. 1999, PASP, 111, 919
Hillebrandt, W., Hoeflich, P., Weiss, A., & Truran, J. W. 1987, Nature, 327, 597
Hoyle, F., & Fowler, W. A. 1960, ApJ, 132, 565
Husemann, B., Jahnke, K., Sánchez, S. F., et al. 2013, A&A, 549, A87
Iglesias-Páramo, J., Vílchez, J. M., Galbany, L., et al. 2013, A&A, 553, L7
Iglesias-Páramo, J., Vílchez, J. M., Rosales-Ortega, F. F., et al. 2016, ApJ, in press [arXiv:1605.03490]
Inserra, C., Pastorello, A., Turatto, M., et al. 2013, A&A, 555, A142
Izotov, Y. I., Stasińska, G., Meynet, G., Guseva, N. G., & Thuan, T. X. 2006, A&A, 448, 955
Kehrig, C., Monreal-Ibero, A., Papaderos, P., et al. 2012, A&A, 540, A11
Kelly, P. L., & Kirshner, R. P. 2012, ApJ, 759, 107
Kelly, P. L., Hicken, M., Burke, D. L., Mandel, K. S., & Kirshner, R. P. 2010, ApJ, 715, 743
Kewley, L. J., & Ellison, S. L. 2008, ApJ, 681, 1183
Kewley, L. J., Dopita, M. A., Sutherland, R. S., Heisler, C. A., & Trevena, J. 2001, ApJ, 556, 121
Kudritzki, R.-P., & Puls, J. 2000, ARA&A, 38, 613
Kuncarayakti, H., Doi, M., Aldering, G., et al. 2013a, AJ, 146, 30
Kuncarayakti, H., Doi, M., Aldering, G., et al. 2013b, AJ, 146, 31
Kuncarayakti, H., Aldering, G., Anderson, J. P., et al. 2015, Publ. Korean Astron. Soc., 30, 139
Leloudas, G., Gallazzi, A., Sollerman, J., et al. 2011, A&A, 530, A95
Levesque, E. M., Soderberg, A. M., Foley, R. J., et al. 2010, ApJ, 709, L26
Liu, Y.-Q., Modjaz, M., Bianco, F. B., & Graur, O. 2015, ArXiv e-prints [arXiv:1510.08049]
Maoz, D., Sharon, K., & Gal-Yam, A. 2010, ApJ, 722, 1879
Marino, R. A., Rosales-Ortega, F. F., Sánchez, S. F., et al. 2013, A&A, 559, A114
Marino, R. A., Gil de Paz, A., Sánchez, S. F., et al. 2016, A&A, 585, A47
Mast, D., Rosales-Ortega, F. F., Sánchez, S. F., et al. 2014, A&A, 561, A129
Maund, J. R., Smartt, S. J., Kudritzki, R. P., Podsiadlowski, P., & Gilmore, G. F. 2004, Nature, 427, 129
Maund, J. R., Fraser, M., Ergon, M., et al. 2011, ApJ, 739, L37
McCully, C., Jha, S. W., Foley, R. J., et al. 2014, Nature, 512, 54
Milisavljevic, D., Margutti, R., Soderberg, A. M., et al. 2013, ApJ, 767, 71
Modjaz, M., Kewley, L., Kirshner, R. P., et al. 2008, AJ, 135, 1136
Modjaz, M., Kewley, L., Bloom, J. S., et al. 2011, ApJ, 731, L4
Mokiem, M. R., de Koter, A., Vink, J. S., et al. 2007, A&A, 473, 603
Moreno-Raya, M. E., Mollá, M., López-Sánchez, Á. R., et al. 2016, ApJ, 818, L19
Moustakas, J., Kennicutt, Jr., R. C., Tremonti, C. A., et al. 2010, ApJS, 190, 233
Neill, J. D., Sullivan, M., Howell, D. A., et al. 2009, ApJ, 707, 1449
Niino, Y., Nagamine, K., & Zhang, B. 2015, MNRAS, 449, 2706
Nomoto, K., Iwamoto, K., Suzuki, T., et al. 1996, in Compact Stars in Binaries, eds. J. van Paradijs, E. P. J. van den Heuvel, & E. Kuulkers, IAU Symp., 165, 119
Pan, Y.-C., Sullivan, M., Maguire, K., et al. 2014, MNRAS, 438, 1391
Panter, B., Jimenez, R., Heavens, A. F., & Charlot, S. 2008, MNRAS, 391, 1117
Papaderos, P., Gomes, J. M., Vílchez, J. M., et al. 2013, A&A, 555, L1
Petrosian, A., Navasardyan, H., Cappellaro, E., et al. 2005, AJ, 129, 1369
Pettini, M., & Pagel, B. E. J. 2004, MNRAS, 348, L59
Pilyugin, L. S., & Mattsson, L. 2011, MNRAS, 412, 1145
Pilyugin, L. S., Vílchez, J. M., & Thuan, T. X. 2010, ApJ, 720, 1738
Podsiadlowski, P., Joss, P. C., & Hsu, J. J. L. 1992, ApJ, 391, 246
Prantzos, N., & Boissier, S. 2003, A&A, 406, 259
Prieto, J. L., Stanek, K. Z., & Beacom, J. F. 2008, ApJ, 673, 999
Prieto, J. L., Lee, J. C., Drake, A. J., et al. 2012, ApJ, 745, 70
Puls, J., Kudritzki, R.-P., Herrero, A., et al. 1996, A&A, 305, 171
Rolleston, W. R. J., Smartt, S. J., Dufton, P. L., & Ryans, R. S. I. 2000, A&A, 363, 537
Rosales-Ortega, F. F., Díaz, A. I., Kennicutt, R. C., & Sánchez, S. F. 2011, MNRAS, 415, 2439
Sahu, D. K., Tanaka, M., Anupama, G. C., Gurugubelli, U. K., & Nomoto, K. 2009, ApJ, 697, 676
Salpeter, E. E. 1955, ApJ, 121, 161
Sana, H., de Mink, S. E., de Koter, A., et al. 2012, Science, 337, 444
Sánchez, S. F., Kennicutt, R. C., Gil de Paz, A., et al. 2012a, A&A, 538, A8
Sánchez, S. F., Rosales-Ortega, F. F., Marino, R. A., et al. 2012b, A&A, 546, A2
Sánchez, S. F., Rosales-Ortega, F. F., Jungwiert, B., et al. 2013, A&A, 554, A58
Sánchez, S. F., Rosales-Ortega, F. F., Iglesias-Páramo, J., et al. 2014, A&A, 563, A49
Sánchez, S. F., Pérez, E., Rosales-Ortega, F. F., et al. 2015, A&A, 574, A47
Sánchez-Menguiano, L., Sánchez, S. F., Pérez, I., et al. 2016, A&A, 587, A70

Sanders, N. E., Soderberg, A. M., Levesque, E. M., et al. 2012, ApJ, 758, 132
Sanders, N. E., Soderberg, A. M., Gezari, S., et al. 2015, ApJ, 799, 208
Sersic, J. L. 1968, Atlas de galaxias australes (Cordoba, Argentina: Observatorio Astronomico)
Shao, X., Liang, Y. C., Dennefeld, M., et al. 2014, ApJ, 791, 57
Singh, R., van de Ven, G., Jahnke, K., et al. 2013, A&A, 558, A43
Smartt, S. J. 2015, PASA, 32, 16
Smith, N., Chornock, R., Li, W., et al. 2008, ApJ, 686, 467
Smith, N., Li, W., Filippenko, A. V., & Chornock, R. 2011, MNRAS, 412, 1522
Stanishev, V., Rodrigues, M., Mourão, A., & Flores, H. 2012, A&A, 545, A58
Stasińska, G. 2006, A&A, 454, L127
Stoll, R., Prieto, J. L., Stanek, K. Z., & Pogge, R. W. 2013, ApJ, 773, 12
Sullivan, M., Conley, A., Howell, D. A., et al. 2010, MNRAS, 406, 782
Taddia, F., Sollerman, J., Razza, A., et al. 2013, A&A, 558, A143
Taddia, F., Sollerman, J., Fremling, C., et al. 2015, A&A, 580, A131
Thöne, C. C., Michałowski, M. J., Leloudas, G., et al. 2009, ApJ, 698, 1307
Tomasella, L., Cappellaro, E., Fraser, M., et al. 2013, MNRAS, 434, 1636
Tsvetkov, D. Y., Pavlyuk, N. N., & Bartunov, O. S. 2004, Astron. Lett., 30, 729
van den Bergh, S. 1997, AJ, 113, 197
van Dyk, S. D. 1992, AJ, 103, 1788
Van Dyk, S. D., Li, W., & Filippenko, A. V. 2003, PASP, 115, 1
Van Dyk, S. D., Davidge, T. J., Elias-Rosa, N., et al. 2012, AJ, 143, 19
Van Dyk, S. D., Zheng, W., Fox, O. D., et al. 2014, AJ, 147, 37
Veilleux, S., & Osterbrock, D. E. 1987, ApJS, 63, 295
Vila-Costas, M. B., & Edmunds, M. G. 1992, MNRAS, 259, 121
Walcher, C. J., Wisotzki, L., Bekeraité, S., et al. 2014, A&A, 569, A1
Yoachim, P., Roškar, R., & Debattista, V. P. 2010, ApJ, 716, L4
Young, D. R., Smartt, S. J., Valenti, S., et al. 2010, A&A, 512, A70
Zaritsky, D., Kennicutt, Jr., R. C., & Huchra, J. P. 1994, ApJ, 420, 87

Appendix A: Disk effective radius (r_e)

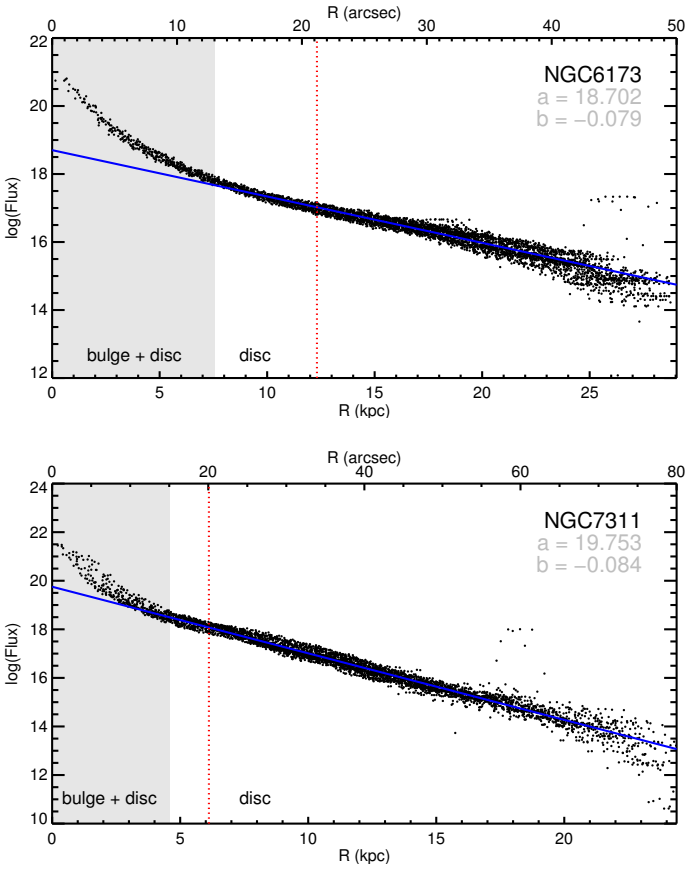

Fig. A.1. Two examples showing the determination of the disk effective radius. The gray shadow defines the region where the bulge contributes to the total surface brightness. This is excluded from the fit, which is performed to the disk profile (solid blue line). The red vertical dotted line corresponds to the disk effective radius, r_e, obtained from the Sérsic profile expression.

The disk effective radius, r_e, is defined as the radius that contains half of the total integrated flux from the disk component. This radius provides a common ruler to properly compare the sizes of the galaxies and the derived quantities at a certain distance. To determine r_e , we performed a morphological decomposition based on the brightness profile. We integrated the flux under the r-band wavelength range in the spectrum of each spaxel and then plotted the logarithm of these measurements against the deprojected GCD, as shown in Fig. A.1 for NGC 6173 and NGC 7311. The contribution of both the central bulge and the disk to the total brightness of the galaxy is clearly visible. This mixture produces a combined surface brightness profile, which can be described by an expression that depends on $r^{1/n}$ (de Vaucouleurs 1948; Sersic 1968; Graham et al. 2005; Galbany et al. 2012)

$$\log I(r) = \log I_0 - 1.6735\ (r/r_e)^{1/n}. \quad (A.1)$$

Depending on the size of the bulge, a different n is needed to properly describe the brightness profile. For example, elliptical galaxies that only have bulge are completely described by the de Vaucouleurs profile $r^{1/4}$ ($n = 4$), while pure disk galaxies are described by a pure exponential profile ($n = 1$). To measure the effective radius of the disk component, we visually determined where the bulge vanishes and fit a pure exponential profile to the disk contribution that excluded the central regions that are dominated by the bulge. Finally, we obtained r_e as the distance at which the logarithm of the flux is 1.6735 lower than the central value of the fit to the disk profile. It is worth noting that fitting a line to these profiles is equivalent to obtaining elliptical rings from the original image because the inclination of the galaxies is taken into account in the deprojection.

We compared the values for the disk effective radii calculated in this work to the values obtained by other works in the CALIFA collaboration. We used two sets of measurements: (i) those measured with a growth curve photometry analysis presented in Walcher et al. (2014); and (ii) those measured in Sánchez et al. (2014), who used a similar procedure to the one presented here. For the galaxies in common (those from the CALIFA mother sample), we obtained similar values (within 10%) for almost all the galaxies. For six galaxies we obtained larger differences, but after repeating the analysis without them, the final results in terms of the common slope did not change significantly when we used the Walcher et al. (2014) or Sánchez et al. (2014) values.

Appendix B: Characteristic metallicity gradient

In this appendix we present the distributions of the metallicity gradient slopes for our SN host galaxy sample. The central decrease was excluded from the metallicity gradient fits, which resulted in different ranges for each galaxy by up to two disk effective radii. The mean metallicity gradient of all 104 galaxies is $-0.016\,(\pm0.013)$ dex kpc^{-1} , with the uncertainty being the standard deviation of the distribution. When the distances are normalized to the disk effective radius r_e, the average gradient becomes $-0.074\,(\pm0.042)$ dex r_e^{-1} (using the O3N2 calibration from M13). The distribution of the normalized gradients is shown in Fig. B.1. We note that the relative scatter of the normalized gradients is smaller than in physical units. In addition, the scatter is fairly low, suggesting a characteristic radial gradient for the oxygen abundance in normalized units. This agrees with the results presented by Sánchez et al. (2012b, 2014), and Sánchez-Menguiano et al. (2016), who reported an average gradient of -0.1 dex r_e^{-1} using the PP04 calibration (we find -0.105 dex r_e^{-1} with that calibration).

The statistics of the distributions using the main calibrator and the comparison methods are presented in Table B.1. The mean values of the distributions of the metallicity gradients for P10 and P11 strong-line methods are around -0.08 dex r_e^{-1}. Five galaxies (UGC 01087, UGC 04036, UGC 4107, NGC 6643, and NGC 3913) have no [O II] line measurement and no P10 abundance estimate can be computed, while IC 0307 and NGC 6166 have no [S II] lines measured and no P11 measurements can be performed. As expected, the distribution of metallicity gradients measured using the N2 calibrator has lower values. This calibrator is not well defined in the high-metallicity regime and the range of allowed values is narrower, which causes the measured gradients to be flatter. We note that although not significant, SNe Ia host galaxies show flatter gradients than both CC SN hosts. The narrower distribution of the O3N2 distribution is also clearly visible.

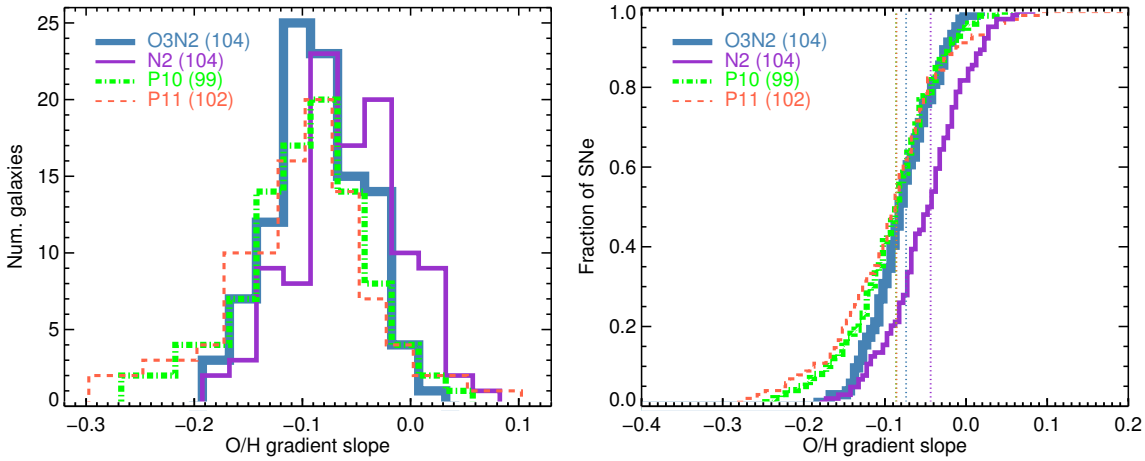

Fig. B.1. Distribution of metallicity gradients using the O3N2 (blue), N2 (purple), P10 (green), and P11 (red) methods. All fits were made considering the errors in each spaxel measurement.

Table B.1. Average values of the metallicity gradient slopes and the standard deviation of the distributions.

	O3N2		N2		P10		P11	
	#	avg.	#	avg.	#	avg.	#	avg.
All Galaxies	104	−0.074 (0.042)	104	−0.044 (0.052)	99	−0.086 (0.059)	102	−0.086 (0.087)
SN Ia hosts	46	−0.064 (0.041)	46	−0 046 (0.050)	43	−0.077 (0.064)	46	−0.077 (0.117)
SN Ibc hosts	27	−0.078 (0.040)	27	−0.040 (0.053)	25	−0.087 (0.050)	26	−0.094 (0.049)
SN II hosts	47	−0.087 (0.037)	47	−0.037 (0.052)	46	−0.091 (0.049)	47	−0.090 (0.050)

Appendix C: Effect of AGNs on the total spectra

The central spectra of about 29% of CC SN hosts, 59% of the star-forming and 100% of the passive SN Ia hosts (see Sect. 4.2.1) in our sample indicate the presence of AGN according to the Kewley et al. (2001) criterion in the BPT diagram[5] (Baldwin et al. 1981; Veilleux & Osterbrock 1987). The emission line measurements from the total spectra of most star-forming galaxies with AGN fall in the star-forming region of the BPT diagram. This indicates that the AGNs are not strong enough to affect the total spectrum significantly. The passive galaxies are an exception because most of the emission comes from the center, and when an AGN is present, its emission may dominate the total emission line spectrum. For this reason, the passive galaxies were not considered when we analyzed the effect of AGNs.

Even though the AGNs in our galaxy sample are not particularly strong, their presence can still affect the metallicity estimates and bias the results from the total spectra. To study this, we obtained two different extractions of the total spectrum for each cube. First, we summed the flux in all the spaxels with a S/N greater than 1.0. As an alternative, we repeated this, but excluded those central spaxels that fall in the AGN region of the so-called BPT diagnostic diagram. The first spectrum would correspond to the spectrum of a galaxy at high redshift or a small galaxy at lower redshift when the whole galaxy falls into the slit or the fiber of the spectrograph.

Figure C.1 shows the gas-phase metallicity estimated from the total spectra with and without the central spaxels falling in the AGN region. All values are close to or above the diagonal, indicating that the metallicity measured from a spectrum including the AGN contribution is usually lower than the measurement

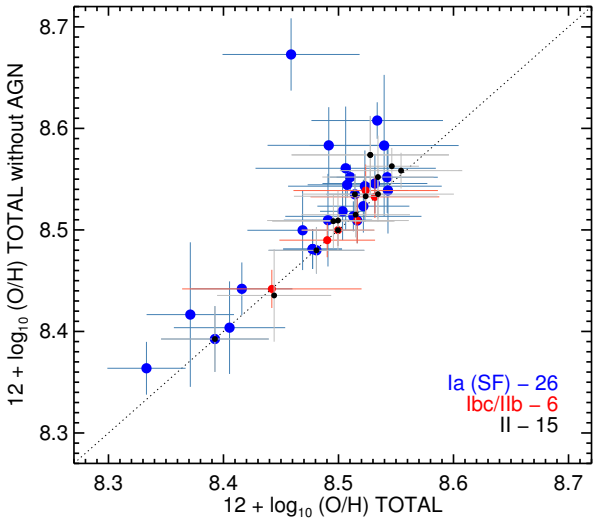

Fig. C.1. Comparison between the average oxygen abundance with and without the AGN contribution.

excluding it. In general, the measurements from the two total spectra for the CC SN hosts agree well. However, for the SN Ia host galaxies the abundances are on average higher by 0.03–0.04 dex when the AGN contribution is removed. This difference raises a potential problem in the metallicity estimation from spectra of high-redshift SN Ia hosts since the presence of a weak AGN contribution might be missed. The metallicity measured from total galaxy spectra should therefore be considered as a lower limit with a systematic error of at least 0.03 dex. However, the AGNs have little effect on the mean total gas-phase metallicity of the galaxies in our sample. When we used the measurement without AGN contribution, the mean metallicity of the SN Ia hosts increased by only 0.012 dex, and no change was observed for CC SN hosts.

[5] Kehrig et al. (2012), Singh et al. (2013) and Papaderos et al. (2013) have shown using CALIFA data that the narrow-line emission that falls in the AGN section of the BPT diagram in some galaxies is not due to AGN activity, but to old post-AGB stars.

Appendix D: Measured quantities

Table D.1. Parameters of the CALIFA galaxies that hosted SNe outside the instrument field of view.

Galaxy	SN name	SN type	AGN	z	OH total	log $(Z_m/Z_\odot)$	Mass $[M_\odot]$
NGC 3184	1921C	I	–	0.001975	8.82	−0.02	10.30
NGC 0477	2002jy	Ia	–	0.019600	8.65	−0.03	10.94
NGC 2487	1975O	Ia	+	0.016148	8.71	−0.05	11.14
NGC 2513	2010ja	Ia	+	0.015561	...	0.12	11.53
NGC 3160	1997C	Ia	+	0.023083	...	−0.06	11.07
NGC 4185	1982C	Ia	–	0.013022	8.73	0.02	11.01
NGC 5485	1982W	Ia	+	0.006428	...	0.10	10.90
NGC 5532	2007ao	Ia	+	0.024704	...	0.11	11.94
NGC 5557	2013gn	Ia	+	0.010737	...	0.16	11.48
IC 1151	1991M	Ia	–	0.007235	8.53	−0.38	10.02
NGC 6027	2006ay	Ia	–	0.014834	8.64	−0.03	11.08
NGC 6411	1999da	Ia	+	0.012695	...	0.04	11.15
NGC 7549	2009nq	Ia	–	0.015799	8.74	−0.22	10.78
NGC 7782	2003gl	Ia	+	0.017942	8.67	0.21	11.44
NGC 3913	1979B	Ia	–	0.003182	8.73	−0.47	9.27
NGC 0171	2009hf	IIP	+	0.013043	8.69	0.09	10.98
NGC 0180	2001dj	IIpec	+	0.017616	8.81	0.02	11.12
NGC 0309	2012dt	II	c	0.018886	8.82	0.05	11.19
NGC 0941	2005ad	IIP	–	0.005364	8.58	−0.34	9.76
UGC 10710	2000bs	IIP	–	0.027976	8.65	0.02	10.87
NGC 1058	1969L	IIP	+	0.001728	8.68	−0.41	9.11
NGC 3184	1937F	IIP	–	0.001975	8.82	−0.02	10.30
NGC 3184	1921B	II	–	0.001975	8.82	−0.02	10.30
NGC 0214	2006ep	Ib	+	0.015134	8.73	0.04	11.30
UGC 04308	1962F	IIb	–	0.011895	8.69	−0.17	10.68
NGC 6060	1997dd	IIb	–	0.014807	8.67	0.04	11.30
NGC 0309	2008cx	IIb	c	0.018886	8.82	0.05	11.19
NGC 0628	2002ap	Ic-bl	c	0.002192	8.69	−0.49	10.30

Table D.2. Type Ia SNe results.

Galaxy	SN name	SN type	AGN	r_e [kpc]	dep-GCD [kpc]	Mass [$M_\odot$]	12 + log (O / H) Gradient [dex r_e^{-1}]	12 + log (O / H) Local	12 + log (O / H) Total	log ($Z_m/Z_\odot$) Local	log ($Z_m/Z_\odot$) Total
NGC 2565	1960M	I	+	4.8	9.4	11.11	−0.082	8.46	8.48	0.04	−0.04
NGC 7319	1971P	I	+	11.1	14.7	11.32	−0.067	...	8.37	...	−0.04
NGC 5668	1954B	Ia	+	3.4	2.2	11.38	−0.108	8.42	8.39	−0.07	−0.10
NGC 3913	1963J	Ia	−	1.4	0.9	9.27	−0.071	8.54	8.53	...	−0.06
NGC 3811	1969C	Ia	−	3.9	2.5	10.79	−0.118	8.54	8.51	0.09	0.18
NGC 7619	1970J	Ia	+	5.3	10.5	11.52	−0.056	...	...	...	−0.40
NGC 4874	1981G	Ia	+	11.9	9.2	11.69	0.013	...	...	0.01	0.10
NGC 1667	1986N	Ia	+	5.6	6.8	11.29	−0.078	8.56	8.51	...	−0.23
NGC 3687	1989A	Ia	+	3.1	4.7	10.43	−0.084	8.47	8.51	...	0.05
NGC 5378	1991ak	Ia	+	6.6	8.1	10.78	−0.037	8.50	8.47	−0.45	−0.51
NGC 0932	1992bf	Ia	+	7.1	4.1	11.26	−0.018	8.42	8.51	0.12	−0.26
UGC 04036	1995E	Ia	+	9.5	5.4	10.94	−0.089	8.57	8.50	0.15	−0.07
NGC 5157	1995L	Ia	+	10.7	9.4	11.33	−0.003	8.54	8.49	0.16	−0.05
NGC 5557	1996aa	Ia	+	4.8	1.4	11.48	−0.114	...	...	...	−0.07
NGC 3982	1998aq	Ia	+	1.2	1.6	10.82	−0.068	8.56	8.51	−0.08	0.22
UGC 00139	1998dk	Ia	−	5.5	1.8	10.18	−0.136	8.52	8.40	0.18	0.10
UGC 01087	1999dk	Ia	c	5.8	8.2	10.65	−0.135	8.47	8.49	...	−0.08
NGC 0495	1999ej	Ia	+	4.1	7.5	10.84	−0.019	...	...	0.22	−0.02
NGC 2623	1999gd	Ia	+	4.2	6.9	10.92	0.018	8.52	8.49	0.22	0.11
UGC 04195	2000ce	Ia	−	6.4	8.0	10.85	−0.091	8.54	8.50	...	−0.06
NGC 0523	2001en	Ia	c	7.4	8.3	10.78	−0.090	8.47	8.45	...	−0.13
UGC 05129	2001fe	Ia	+	3.8	3.6	10.63	−0.075	8.58	8.52	...	−0.41
2MFGC 13321	2002aw	Ia	+	4.8	3.2	10.76	−0.053	8.48	8.54	...	−0.06
NGC 7253	2002jg	Ia	−	13.1	7.3	10.80	0.003	8.54	8.55	0.18	0.05
MCG -02-02-086	2003ic	Ia	+	18.4	10.9	11.91	−0.130	...	...	−0.11	−0.31
UGC 00005	2003lq	Ia	+	11.0	19.2	11.27	−0.101	...	8.51	0.13	0.07
UGC 10097	2004di	Ia	+	11.4	22.0	11.32	−0.035	...	8.46	0.11	0.06
NGC 1060	2004fd	Ia	+	7.0	2.1	11.86	−0.023	...	...	−0.46	−0.26
MCG -01-09-006	2005eq	Ia	c	10.7	21.7	11.24	−0.101	8.47	8.49	−0.25	−0.19
NGC 7311	2005kc	Ia	+	6.1	5.9	10.77	−0.089	8.58	8.52	−0.03	0.04
UGC 04468	2006bb	Ia	+	20.2	14.8	11.34	0.030	...	...	−0.02	0.11
NGC 5587	2006dy	Ia	+	3.7	6.0	10.58	−0.024	8.53	8.53	0.16	−0.07
CGCG 207-042	2006te	Ia	−	6.5	6.3	10.50	−0.075	8.56	8.46	...	−0.41
NGC 0105	2007A	Ia	+	4.2	3.6	10.88	−0.106	8.60	8.48	...	−0.49
UGC 04008	2007R	Ia	c	10.4	3.0	11.37	−0.026	8.56	8.55	...	−0.49
NGC 2577	2007ax	Ia	+	3.3	1.5	10.88	−0.063	...	...	...	−0.51
UGC 04455	2007bd	Ia	+	8.2	6.3	11.15	−0.053	8.58	8.54	−0.53	−0.65
NGC 7469	2008ec	Ia	+	3.7	5.2	11.36	−0.001	8.48	8.42	0.21	0.18
NGC 6166	2009eu	Ia	+	11.5	20.9	11.37	−0.008	...	...	0.15	0.08
NGC 5525	2009gt	Ia	−	12.2	28.1	11.33	−0.112	...	8.50	...	−0.33
NGC 6146	2009fl	Ia	+	8.8	7.7	11.62	−0.049	...	...	−0.62	−0.43
NGC 6173	2009fv	Ia	+	12.3	5.8	11.86	−0.011	...	...	−0.01	0.14
NGC 7364	2009fk	Ia	c	4.9	2.6	10.80	−0.018	8.58	8.57	0.02	0.04
UGC 11975	2011fs	Ia	−	5.2	16.8	10.81	−0.045	...	8.56	...	0.05
NGC 7364	2011im	Ia	c	4.9	9.7	10.80	−0.018	8.57	8.57	...	0.16
NGC 5421	2012T	Ia	c	6.8	3.0	11.33	−0.049	8.52	8.51	−0.09	0.08
NGC 5611	2012ei	Ia	+	2.2	2.1	10.38	−0.076	...	...	0.09	0.09
UGC 08250	2013T	Ia	−	7.3	12.6	10.31	−0.064	8.39	8.39	...	−0.16
NGC 7321	2013di	Ia	+	7.6	12.2	10.73	−0.103	8.53	8.52	0.12	0.04
NGC 2554	2013gq	Ia	+	6.0	2.6	11.39	−0.009	8.50	8.41	...	0.03
NGC 6166	PS15aot	Ia	+	11.5	5.4	11.37	−0.008	...	...	...	0.14
NGC 0938	2015ab	Ia	+	5.1	3.8	11.12	−0.013	8.43	8.34	...	−0.33
UGC 03151	1995bd	Ia-pec	+	6.0	7.1	11.06	−0.011	8.59	8.53	0.16	0.07
NGC 0105	1997cw	Ia-pec	+	4.2	3.5	10.88	−0.106	8.56	8.48	0.03	0.15
NGC 2595	1999aa	Ia-pec	−	9.1	8.2	11.18	−0.038	8.45	8.51	0.19	0.17
NGC 6063	1999ac	Ia-pec	c	5.1	7.7	10.39	−0.120	...	8.48	−0.11	0.13
NGC 0976	1999dq	Ia-pec	+	7.5	2.6	11.15	−0.030	8.62	8.54	0.02	0.07
NGC 2691	2011hr	Ia-pec	c	5.7	2.1	10.68	−0.055	8.56	8.49	0.16	0.04

Table D.3. Type II SNe results.

Galaxy	SN	SN type	AGN	$r_{\rm eff}$	dep-GCD	Mass	12 + log (O/H)			Z_m	
							grad	local	total	local	total
NGC 3811	1971K	II	–	3.9	7.6	10.79	−0.118	8.50	8.51	−0.16	−0.40
NGC 2565	1992I	II	+	4.8	13.3	11.11	−0.082	8.60	8.48	−0.01	0.10
NGC 3057	1997cx	II	–	3.6	1.7	9.51	−0.095	8.33	8.28	0.09	−0.06
NGC 2916	1998ar	II	+	7.8	10.8	11.07	−0.135	...	8.50	...	−0.39
UGC 03555	1999ed	II	–	4.7	6.4	11.12	−0.134	8.50	8.46	0.09	0.10
NGC 0309	1999ge	II	c	12.0	6.8	11.19	−0.087	8.70	8.60	−0.03	0.04
UGC 05520	2000L	II	–	5.3	6.6	10.03	−0.180	8.33	8.37	0.15	0.06
UGC 00005	2000da	II	+	11.0	7.7	11.27	−0.101	8.61	8.51	0.05	−0.21
MCG -01-10-019	2001H	II	–	8.8	3.2	10.40	−0.123	8.56	8.46	0.04	0.06
NGC 2604	2002ce	II	–	3.4	3.0	10.05	−0.092	8.33	8.38	0.07	0.22
NGC 7771	2003hg	II	–	3.7	3.6	11.28	−0.055	8.61	8.50	−0.40	0.01
UGC 00148	2003ld	II	–	7.5	2.5	10.24	−0.040	8.43	8.40	−0.67	−0.63
NGC 5668	2004G	II	+	3.4	5.6	11.38	−0.108	...	8.39	−0.04	0.10
NGC 5980	2004ci	II	c	5.5	6.1	11.12	−0.120	8.56	8.53	−0.47	−0.09
NGC 6786	2004ed	II	–	5.2	5.3	11.54	−0.089	8.55	8.55	0.10	0.10
NGC 5056	2005au	II	c	6.6	8.1	11.00	−0.122	8.43	8.45	0.14	0.13
NGC 5682	2005ci	II	–	3.4	1.9	9.54	−0.083	8.32	8.35	...	0.06
NGC 5630	2005dp	II	–	3.3	4.8	9.89	−0.057	8.35	8.32	...	0.03
UGC 04132	2005en	II	–	8.1	6.8	11.34	−0.104	8.46	8.51	0.07	0.13
NGC 0774	2006ee	II	+	7.8	4.8	10.42	−0.161	8.50	8.44	0.04	0.05
NGC 5888	2007Q	II	+	11.2	12.6	11.41	−0.053	8.56	8.53	...	0.22
NGC 6643	2008ij	II	–	4.5	3.0	10.46	−0.101	8.53	8.52	0.20	0.10
NGC 5888	2010fv	II	+	11.2	9.1	11.41	−0.053	8.68	8.53	0.13	−0.08
NGC 1056	2011aq	II	c	2.6	0.7	10.57	−0.075	8.49	8.44	−0.38	−0.15
NGC 5425	2011ck	II	–	2.7	2.8	9.83	−0.113	8.42	8.38	0.07	0.17
NGC 5732	ASASSN-14fj	II	–	4.8	8.3	10.33	−0.162	8.36	8.47	−0.24	0.04
NGC 5406	PSN J14002117 +3854517	II	+	7.1	2.0	11.22	−0.072	8.50	8.54	...	0.20
IC 0758	1999bg	IIP	–	1.8	3.4	9.32	−0.049	8.35	8.43	0.21	−0.02
NGC 1637	1999em	IIP	c	2.5	1.1	9.74	−0.020	8.64	8.58	0.22	0.08
NGC 3184	1999gi	IIP	–	2.2	2.5	10.30	−0.057	8.63	8.60	...	−0.02
NGC 2347	2001ee	IIP	+	4.6	6.2	11.19	−0.093	8.52	8.51	0.05	0.17
NGC 5772	2002ee	IIP	+	7.5	12.9	10.52	−0.069	8.44	8.52	0.17	0.03
NGC 0628	2003gd	IIP	c	3.2	7.3	10.29	−0.132	8.48	8.51	...	0.14
NGC 1093	2009ie	IIP	+	6.5	16.2	10.96	−0.074	8.49	8.50	0.05	0.20
UGC 09356	2011cj	IIP	–	2.4	2.6	9.88	−0.081	8.40	8.42	−0.10	0.01
NGC 0628	2013ej	IIP	c	3.2	7.4	10.29	−0.132	...	8.51	0.20	0.01
NGC 7691	2014az	IIP	–	8.2	7.8	10.50	−0.025	8.45	8.49	−0.16	−0.32
UGC 10123	2014cv	IIP	c	4.0	2.7	10.68	−0.044	8.53	8.50	−0.09	0.16
UGC 01635	2003G	IIn	c	6.1	2.8	10.42	−0.025	8.64	8.56	0.19	0.12
NGC 0214	2005db	IIn	+	7.1	5.6	11.30	−0.033	8.68	8.53	−0.08	0.06
NGC 2906	2005ip	IIn	+	3.2	4.0	10.91	−0.081	8.40	8.55	0.02	0.01
NGC 5630	2006am	IIn	–	3.3	2.7	9.89	−0.057	8.31	8.32	...	−0.00
NGC 4644	2007cm	IIn	+	4.2	8.4	10.84	−0.052	8.51	8.53	0.05	0.09
NGC 5829	2008B	IIn	–	6.3	9.0	10.33	−0.098	8.50	8.46	0.19	0.17
UGC 09842	2012as	IIn	c	11.0	20.1	10.90	−0.087	8.46	8.50	−0.40	−0.28
UGC 04132	2014ee	IIn	–	8.1	10.1	11.34	−0.104	8.47	8.51	...	−0.32
NGC 1058	1961V	II-pec	+	1.0	2.7	9.11	−0.072	8.23	8.50	0.15	0.16

Table D.4. Type Ibc/IIb SNe results.

Galaxy	SN	SN type	AGN	$r_{\rm eff}$	dep-GCD	Mass	12 + log (O/H)			log ($Z_m/Z_\odot$)	
							grad	local	total	local	total
NGC 3655	2002ji	Ibc	c	1.8	3.0	10.74	−0.064	8.54	8.55	−0.49	−0.47
NGC 5714	2003dr	Ibc	–	4.8	7.8	10.26	−0.079	8.39	8.49	−0.03	−0.35
UGC 06517	2006lv	Ibc	–	3.0	2.6	10.04	−0.130	8.52	8.46	...	−0.11
UGC 02134	2011jf	Ibc	c	6.6	0.9	11.02	−0.028	8.58	8.52	...	−0.07
UGC 04107	1997ef	Ibc-pec	–	5.9	5.4	10.82	−0.096	8.50	8.52	−0.25	−0.24
NGC 5559	2001co	Ibc-pec	c	6.2	7.8	11.10	−0.088	8.56	8.48	0.16	−0.11
NGC 0991	1984L	Ib	+	3.8	4.3	9.63	−0.142	8.43	8.44	0.22	0.09
NGC 5480	1988L	Ib	–	3.1	1.9	10.34	−0.045	8.58	8.55	−0.26	0.01
NGC 0776	1999di	Ib	c	8.0	5.9	11.16	−0.076	8.67	8.59	0.19	0.06
NGC 2596	2003bp	Ib	–	8.7	9.2	11.16	−0.123	8.51	8.49	0.11	0.01
NGC 7364	2006lc	Ib	c	4.9	4.2	10.80	−0.018	8.57	8.57	0.09	−0.19
NGC 6186	2011gd	Ib	–	4.2	0.6	10.77	−0.039	8.60	8.58	0.04	0.09
UGC 05100	2002au	IIb	–	4.6	7.9	11.18	−0.058	8.50	8.50	0.19	0.11
IC 0307	2005em	IIb	c	11.7	12.1	11.34	−0.077	...	8.49	...	−0.20
NGC 5735	2006qp	IIb	+	5.7	9.3	10.75	−0.139	8.40	8.49	0.07	−0.05
NGC 6643	2008bo	IIb	–	4.5	3.7	10.46	−0.101	...	8.52	−0.03	0.02
NGC 1070	2008ie	IIb	+	6.2	8.7	11.13	0.020	8.63	8.52	0.05	−0.20
UGC 10331	2011jg	IIb	–	5.8	6.7	10.36	−0.072	8.39	8.37	...	−0.04
NGC 3310	1991N	Ic	c	1.5	0.6	10.13	−0.027	8.35	8.33	−0.07	0.03
MCG -01-54-016	2001ch	Ic	–	4.4	4.4	9.19	−0.065	8.12	8.24	...	0.10
NGC 4210	2002ho	Ic	+	4.3	3.5	10.59	−0.097	8.56	8.53	...	0.22
NGC 5000	2003el	Ic	c	6.2	6.6	11.08	−0.048	8.58	8.53	−0.02	−0.13
UGC 03555	2004ge	Ic	–	4.7	2.0	11.12	−0.134	8.58	8.46	0.22	0.14
NGC 4961	2005az	Ic	–	3.0	1.8	10.03	−0.104	8.49	8.44	0.16	0.17
UGC 04132	2005eo	Ic	–	8.1	9.9	11.34	−0.104	8.49	8.51	0.20	0.20
NGC 1058	2007gr	Ic	+	1.0	1.0	9.11	−0.072	8.54	8.50	...	−0.59
NGC 7321	2008gj	Ic	+	7.6	17.8	10.73	−0.103	8.39	8.52	...	0.02